D I P L O M A R B E I T

Selective Oxidation of Ethanol on Supported AuAg Bimetallic Catalysts

Ausgeführt am

Institut für Materialchemie
der Technischen Universität Wien

unter der Anleitung von

Univ. Prof. Dr. rer. nat. Günther Rupprechter und
Dr. techn. Karin Föttinger als verantwortlich mitwirkender
Universitätsassistentin

durch

Matthäus Rothensteiner
Pfeilgasse 3a
1080 Wien

Wien, 5. April. 2012

Danksagung

An dieser Stelle möchte ich allen herzlich danken, die mich bei der Erstellung meiner Diplomarbeit unterstützt haben.

Prof.Günther Rupprechter danke ich für die Möglichkeit die Diplomarbeit in seiner Forschungsgruppe zu verfassen.

Dr. Karin Föttinger danke ich für die interessante und abwechslungsreiche Themenstellung, die Möglichkeit auch im Ausland Messdaten und Erfahrung zu sammeln, sowie für die exzellente Betreuung von der praktischen Durchführung der Messungen bis hin zur Diskussion der Ergebnisse und der raschen Korrektur der Arbeit.

Weiters gilt mein Dank DI Andreas Haghofer für seine Unterstützung bei der experimentellen Arbeit und der Auswertung von Messdaten; Dr. Christian Weilach und DI Harald Holzapfel für die Durchführung der XPS Messungen und Konrad Kainz für seinen Beitrag zu den Kinetikmessungen.

Bei meinen Kollegen der Arbeitsgruppe und den Mitarbeitern des Instituts für Materialchemie möchte ich mich für die Unterstützung in technischen als auch in administrativen Belangen sowie für die angenehme Arbeitsatmosphäre bedanken.

Bei meinen Freunden möchte ich mich für die Ablenkung vom Ernst des Studiums durch gemeinsame sportliche und kulturelle Aktivitäten bedanken. Jenen, die mit mir das Studium absolviert haben, danke ich besonders für die gegenseitige Motivation und Hilfe.

Der größte Dank gilt jedoch meiner Familie: meinen Geschwistern und besonders meinen Eltern, die mir das Studium überhaupt erst ermöglicht haben.

Abstract

The aim of this thesis was the synthesis and characterization of mono- and bimetallic Au and AuAg nanoparticles supported on TiO_2 and ZrO_2 as catalyst for the selective gas-phase partial oxidation of ethanol.

The main characterization methods were transmission electron microscopy, X-ray absorption spectroscopy, IR spectroscopy with CO as probe molecule, X-ray photoelectron spectroscopy and kinetic measurements. These methods allowed the investigation of the morphology, oxidation states, adsorption properties, surface composition and reactivity of the catalysts.

Samples with 2 and 4 % Au loading and a Au/Ag molar ratio of 4/1 were prepared using deposition-precipitation (Au) and incipient wetness impregnation (Ag).

All catalysts showed promising catalytic properties for aldehyde formation. At 200 °C and an ethanol/O_2 ratio of 1/1 ethanol conversion on bimetallic TiO_2 catalysts was superior to monometallic Au catalyst. Acetaldehyde is formed at selectivities up to 98 %; ethylacetate is the main byproduct. Upon exposure to reaction conditions at 300 °C, irreversible deactivation most probably due to morphology changes occured.

A significant change in particle size was absent after use at 200 °C. Particle size distributions determined by TEM yielded similar values for mono- and bimetallic catalysts. A strong dependence of particle size from H_2 flow rates during reduction of TiO_2 based catalysts was observed.

For characterization of structure and alloy formation, operando XAS measurements at the Ag K edge and Au L_{III} edge were performed during reduction and reaction of bimetallic TiO_2 catalysts. The interaction of Ag with O_2 is reflected in the Ag K edge XANES. Evidence of alloy formation could be found by the determination of Ag-Au and Ag-Ag coordination numbers from the Ag K edge EXAFS.

Besides bulk structure, more surface sensitive characterization methods were applied. In situ FTIR CO adsorption measurements showed the emergence of an absorption band at 2055 cm^{-1}. We propose the assignment of this band to CO coordinated to Au on negatively charged clusters due to interaction with the reducible TiO_2 support or the presence of Ag. Small differences between the mono-and bimetallic catalysts were observed in the spectral range typical of bridge-bonded CO.

XPS measurements indicated an elevated surface concentration of Ag and evidence that oxidised Au might be present under reaction conditions.

Zusammenfassung

Ziel dieser Arbeit war die Synthese und Charakterisierung von mono- und bimetallischen Au und AuAg Nanopartikeln auf TiO_2 und ZrO_2 als Katalysatoren für die selektive partielle Gasphasenoxidation von Ethanol.

Als Charakterisierungsmethoden wurden Transmissionselektronenmikroskopie, Röntgenabsorptionsspektroskopie, IR Spektroskopie mit CO als Sondenmolekül, Röntgenphotoelektronenspektroskopie und kinetische Messungen eingesetzt, welche die Untersuchung von Reaktivität, Morphologie, Oxidationszustand, Adsorptionseigenschaften, sowie der Oberflächenzusammensetzung erlauben.

Mittels Deposition-Präzipitation (Au) und Trockenimprägnierung (Ag) wurden Proben mit 2 und 4 % Au und einem Au/Ag Verhältnis von 4/1 hergestellt.

Alle Katalysatoren zeigten vielversprechende kinetische Eigenschaften bezüglich der Acetaldehydbildung. Bei 200 °C und einem Ethanol/O_2 Verhältnis von 1/1 zeigten die monometallischen Au Katalysatoren einen niedrigeren Ethanolumsatz als die bimetallischen. Acetaldehyd wird mit Selektivitäten von bis zu 98 % gebildet; Ethylacetat ist das häufigste Nebenprodukt. Irreversible Deaktivierung bei 300 °C und Reaktionsbedingungen tritt vermutlich nicht durch Sintern sondern durch Morphologieänderungen auf.

Reaktionsbedingungen bei 200 °C führten zu keiner signifikanten Änderung der Teilchengröße. Mit TEM ermittelte Teilchengrößenverteilungen ergaben ähnliche Werte für die mono- und bimetallischen Katalysatoren. Eine starke Abhängigkeit der Teilchengröße vom H_2 Fluß bei der Reduktion von TiO_2 geträgerten Katalysatoren wurde beobachtet.

Zur Charakterisierung von Struktur und Legierungsbildung wurden operando XAS Messungen an der Ag K Kante und Au L_{III} Kante an den bimetallischen TiO_2 geträgerten Katalysatoren durchgeführt. Hinweise auf die Wechselwirkung von Ag und O_2 konnten im Ag XANES beobachtet werden. Der Nachweis einer Legierungsbildung erfolgte durch Bestimmung von Ag-Au und Ag-Ag Koordinationszahlen.

Auch besonders oberflächensensitive Methoden wurden verwendet. In situ FTIR Messungen der CO Adsorption zeigten die Bildung einer Absorptionsbande bei 2055 cm^{-1}. Aufgrund der Reduzierbarkeit von TiO_2 könnte diese durch CO Adsorption auf negativ geladenen Au Clustern erklärt werden. Zwischen mono- und bimetallischen Katalysatoren wurden geringe Unterschiede im für an Brückenplätzen adsorbiertes CO typischen Spektralbereich gefunden.

XPS Messungen zeigten eine erhöhte Oberflächenkonzentration an Ag und Hinweise auf das Vorliegen von oxidiertem Au unter Reaktionsbedingungen.

Contents

Chapter 1

Introduction

Gold is the most noble transition metal, one of the few colored metals and among the least reactive solid elements. The metal with the yellow, lustrous color that occurs in its free elemental form has fascinated mankind since the dawn of civilization. In modern technology, its high resistance to corrosion, high electric conductivity and excellent reflecting properties in the infrared region account for its importance. Gold is the most ductile and soft metal and it possesses 70 % of the electric conductivity of silver.
For a long time, little attention was paid to its chemistry as it forms comparatively few compounds, many of which are stable only at very low temperatures. The chemistry of gold comprises compounds with gold in the -I to +V oxidation states with Au(I) and Au(III) coordination compounds exhibiting the highest stability. Au(III) is a strong oxidizing agent and shows a high tendency to form quadratically coordinated complexes.

While Au is inert as a bulk material, clusters and particles with diameters in the nanometer-range are surprisingly active catalysts. Two independent discoveries in the 1980s have initiated a lot of research in the field of Au catalysis: Firstly, Hutchings discovered that heterogeneous gold catalysts are highly active in the hydrochlorination of acetylene [1] and secondly, Haruta revealed the high catalytic activity of nanoparticulate Au in the oxidation of CO even far below room temperature [2]. Homogeneous and heterogeneous Au catalysts exhibit exceptional properties in many reactions.
CO oxidation, a prototype reaction for mechanistic studies, is the most extensively studied reaction over supported Au catalysts. The reaction mechanism of oxidation reactions over Au catalysts is unknown and there is a vivid debate about the nature of the active site, involving concepts like cationic as well as anionic gold and models in which the support material plays a central role [3].

Selective oxidation is one of the major pathways by which chemical feedstocks are activated and plays a key role in the production of a great number of intermediates and products. However, due to the absence of selective catalysts many oxidation processes are inefficient.

From the ecological perspective, many oxidation methods are undesirable because they use stoichiometric oxidizing agents such as chromates and permanganates or halooxoacids. Therefore, these processes should be replaced by environmentally benign, atom-efficient catalytic processes that are ideally performed under mild and solvent-free conditions with molecular oxygen as oxidizing agent. Hence, there is urgent need of the development of heterogeneously catalyzed oxidation reactions using gas or liquid phase reagents.

Supported nanocrystalline gold is a promising candidate for heterogeneously catalyzed oxidation processes, in particular for the selective oxidation of alcohols, which represents a demanding target. Advances in the field of gold catalysis have been reviewed by Bond and Thompson [4], Zhan and Thompson [3], Haruta and Hutchings [5], Edwards et al. [6], Chen and Goodman [7], Corma and Garcia [8], Hashmi and Hutchings [9], Hashmi and Rudolph [10], Hutchings [5, 11, 12, 13, 14, 15, 16, 17], Della et al. [18], Matsumoto et al. [19] and Dimitratos et al. [20].

Oxygen activation is a crucial step in oxidation reactions. DFT (density functional theory) calculations of molecular O_2 adsorption on Au supported on TiO_2 performed by Boronat and Corma [21] indicated that particle morphology is a key factor because the lowest activation barriers for O_2 dissociation were found in bridge-bridge conformations that are only stable on Au (1 0 0) facets. However, the most active sites were found at the metal-support interfaces and not on the gold particle. In another study it was shown that the activity of Au catalysts in alcohol dehydrogenation to aldehydes depends on the coordination number of surface Au atoms: The lower the coordination number, the higher the reactivity. Therefore, smaller Au particles are more active catalysts [22].

The catalytic properties of gold can be promoted by the addition of silver. Ag is a very active catalyst for oxidation reactions, also in CO oxidation, however at higher temperatures than Au. Supported Ag catalysts are used on an industrial scale in the direct oxidation of ethene to oxirane or the dehydrogenation of methanol. Liu et al. [23] found that the catalytic activity of Au nanoparticles is promoted by alloying with Ag. The catalytic activity of core-shell nano-particles surpassed that of monometallic and alloy nano-particles. Zhang et al. [24] reported superior catalytic activity of col-

loidal Au@Ag nanoparticles in aerobic glucose oxidation and Jiang et al.[25] found the same effect in Au@Ag nano-particles supported on a metal-organic framework (MOF) in the reduction of 4-nitrophenol.
Bulk Au and Ag form a continuous series of solutions both in the liquid and crystalline phases. This property also prevails at particle sizes in the nanometer-range [26], however there is evidence of the segregation of Ag to the surface of AuAg alloys [27, 28].

Nowadays, about 95 % of carbon-containing high-tonnage commodity chemicals are based on fossile carbon resources. Decreasing oil reserves and the greenhouse problem necessitate the development of sustainable sources of organic chemical compounds.

Ethanol produced from biomass is used as a fuel and fuel additive on an increasingly large scale. Besides, bioethanol has attracted much attention as a renewable feedstock for a number of bulk chemicals such as acetaldehyde, acetic acid, ethene and butadiene [29]. It has been demonstrated that a number of primary and secondary alcohols, polyols and aldehydes can be selectively oxidized over supported gold catalysts under mild conditions. Most of this research focussed on applications in the liquid phase where acids [30, 29, 31], and esters [32] are formed. In the gas phase oxidation of ethanol on Au catalysts the product composition depends on the nature of the support material [33].

The aim of this thesis was to study TiO_2 supported Au and AuAg catalysts in the gas phase oxidation of ethanol and to investigate the effect of Ag addition to Au. Kinetic measurements were performed to compare the reactivity of different catalysts. Especially interesting is the investigation of the internal structure of the bimetallic particles by X-ray absorption spectroscopy (XAS) under reaction conditions. Further characterization was performed by transmission electron microscopy (TEM), CO adsorption using in situ Fourier transform infrared spectroscopy (in situ FTIR) and X-ray photoelectron spectroscopy (XPS).

Chapter 2

Theoretical Background

2.1 Preparation Methods

It is still difficult to design a catalytically active material with predefined properties. In the preparation and pretreatment methods, a large number of parameters occur and upon small changes thereof, the catalytic properties can change considerably.

Heterogeneous catalysis takes place on the surface of a catalytically active phase and therefore, a big surface area is demanded to reduce the amount of catalyst and boost the catalytic activity.
Two main strategies to disperse the catalytically active phase on a carrier material can be distinguished: Firstly, to incorporate it already in the preparation of the support itself (e.g. by sol-gel methods or spray pyrolysis) and, secondly, to add the metal to a support material by impregnation, ion exchange, adsorption or deposition-precipitation. The support should provide a high surface area and stabilize the nano-particles. In many cases, the nature of the support affects the catalytic activity. In the following, the methods that were used in this work are described.

Deposition-Precipitation

Deposition-Precipitation (DP) involves two steps: precipitation and interaction with the support surface. In this method, precipitation in the bulk solution outside the pores of the support must be avoided. Ideally, the OH-groups of the support directly interact with the ions present in the solution. The nucleation rate must be higher at the surface than in the bulk solution and the homogeneity of the solution must be preserved. In order to obtain uniform precipitation, urea can be used instead of alkali bases. Urea decomposes slowly in aqueous solution, which leads to a uniform concentration of

OH^- in the bulk and pore solutions. Hence, the precipitation of metal hydroxide due to local increase in pH is avoided and precipitation occurs evenly over the support surface.
The deposition-precipitation of Au on TiO_2 described by Zanella et al. [34, 35, 36, 37] allows the synthesis of small Au particles at higher loadings and high yields up to 100% can be obtained. The orange precipitate that is deposited on TiO_2 is an amorphous Au(III) compound with an atomic composition of $AuN_{2.2}O_{1.2}C_{0.9}H_{4.2}Cl_{0.1}$.

Incipient Wetness Impregnation

Incipient wetness impregnation (IWI) is a commonly used method in the synthesis of supported heterogeneous catalysts and makes use of capillary action. A solution of a metal precursor is prepared and added to the support material in such a way that the amount of solution equals the pore volume of the catalyst support. The distribution of the impregnated compound depends on the mass transfer conditions within the pores during impregnation and drying. The maximum loading is limited by the solubility of the precursor in the solution [38].

2.2 Support Materials

2.2.1 Properties of TiO_2

TiO_2 crystallizes in three major structures: rutile, anatase and brookite. Only the tetragonal rutile and anatase structures play a role in the applications of TiO_2. The most striking example of its use might be as a white pigment due to its high refractive index. In the rutile and anatase modifications, six oxygen atoms surround one titanium atom in a more or less distorted octahedral configuration.
TiO_2 is a typical transition metal oxide: It is easily reducible and the titanium-oxygen phase diagram includes a large number of compounds with mixed oxidation states and non-stoichiometry.
Oxygen atoms can be removed reversibly from TiO_2 by treatment with hydrogen. This induces the formation of a dark blue non-stoichiometric rutile phase $TiO_{(2-x)}$ with various defects containing Ti(III) and Ti(IV) species. The rutile (1 1 0) surface is the most stable crystal face of TiO_2 [39].
TiO_2 is an amphoteric oxide with an isoelectric point (IEP) of 6. The IEP is the pH at which the surface carries no net electrical charge. Since the surface charge of an oxide immersed in a solution depends on its IEP, and the pH

and ion strength of the solution, in case of pH(solution) > IEP_{TiO_2}, the surface is negatively charged (main surface species O^-), whereas the surface is positively charged (main surface species OH^+) if pH(solution) < IEP_{TiO_2} [34].

TiO_2 is a very common support material in heterogeneous catalysts, e.g in selective catalytic reduction (SCR) processes like the treatment of diesel engine exhaust gas. TiO_2 is among the most important supports of Au catalysts owing to its ability to stabilize small Au particles.
TiO_2 is an indirect semiconductor (bandgap 3,0 eV rutile; 3.2 eV anatase) and a very active photocatalyst. Upon irradiation with sunlight, an electron-hole pair is created and the charge carriers might migrate to the surface. There they react with adsorbed water and oxygen to radical species that can oxidize organic molecules. Unfortunately, TiO_2 has a low quantum yield for the photochemical conversion of solar energy. However, a noteworthy improvement in efficiency was achieved in dye-sensitized solar cells [39].

2.2.2 Properties of ZrO_2

Compared to TiO_2, low oxidation states of Zr in ZrO_2 are less stable and ZrO_2 exhibits a more basic character. At room temperature, ZrO_2 exhibits a monoclinic crystal structure with 7 oxygen atoms coordinated to zirconium. Excellent mechanical and thermal properties can be achieved by stabilizing the high-temperature cubic phase by addition of dopants like yttria. In addition, anion vacancies are generated: Doped ZrO_2, e.g. yttria stabilized zirconia (YSZ) is a pure anionic conductor and widely used in ceramic fuel cells. Due to its high thermal stability, zirconia is also used as support material for heterogeneous catalysts in high temperature applications like exhaust gas purification.
Besides, ZrO_2 has been applied as a catalyst itself in the hydrogenation and isomerisation of olefins or the dehydration of alcohols. The surface of ZrO_2 exhibits four chemical properties, namely acidic, basic, oxidizing and reducing. The bifunctional acid-base properties are reflected in the capacity to chemisorb both CO_2 and NH_3. Surface acid and base properties are rather weak, but they work independently and/or cooperatively in catalytic processes.
Adsorption of carbon dioxide on monoclinic zirconia yields hydrogen carbonates and monodentate and bidentate carbonates, suggesting that its surface basicity is due to terminal hydroxyl groups,coordinatively unsaturated O^{2-} centers and Zr^{4+} - O^{2-} pairs [40]. The isolelectric point of ZrO_2 is higher than that of TiO_2 [41].

2.3 X-Ray Absorption Fine Structure

X-ray absorption fine structure (XAFS) is based on the absorption of X-rays at energies near and above the core-level binding energies of an atom. Since the absorption probability is a function of the nature of the immediate vicinity of the absorbing atom, XAFS provides local information about its chemical and physical state. XAFS has been used for almost 40 years in the field of catalysis [42] and has proven to be a powerful method as it places few constraints on the nature of the sample. XAS exclusively probes photons. Thus, it is ideally suited for measurements under "real" reaction conditions, also referred to as operando spectroscopy. Since XAFS requires intense, energy-tunable X-ray radiation, its application is limited and its development is closely linked to that of synchrotrons.

The method is only limited by the weak interaction of X-rays with light

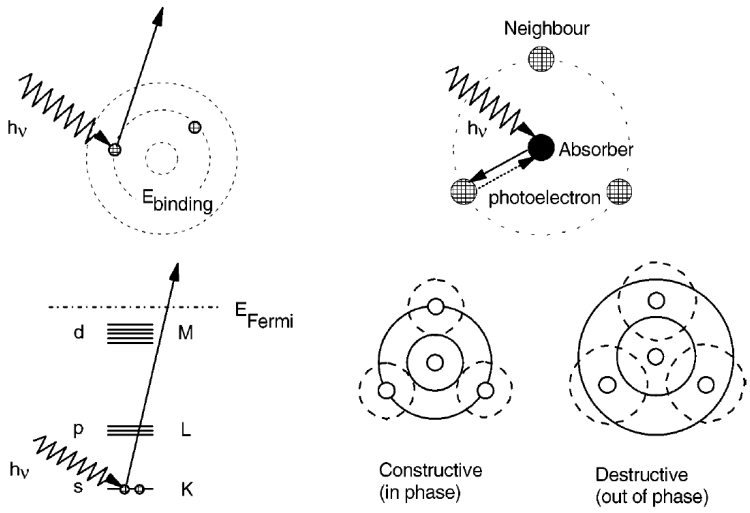

Figure 2.1. (a) Illustration of the photoelectric effect and (b) interference of the outgoing and backscattered photo-electron wave at an absorbing atom. Reproduced from [43].

elements. Due to the fact that XAFS is an atomic probe, crystallinity is not required and the investigation of highly disordered materials is possible. Providing information about the average local structure, XAFS is a powerful complementary technique to diffraction techniques.

In catalysis, surface sensitivity is essential but it is limited in XAFS due to the ability of X-rays to penetrate matter. However, as catalysts commonly are highly dispersed materials with small particle sizes, a great fraction of the signal is generated by surface atoms.

2.3.1 Physical Principles

The extent of the attenuation of radiation passing through a material is described by the Lambert-Beer law (2.1) which states that the absorbance A linearly depends on the optical path x and the linear absorption coefficient $\mu(E)$, which is a function of the photon energy.

$$A = log\frac{I_0}{I_T} = \mu(E)x \tag{2.1}$$

Within the dipole approximation, the probability of the transition of a core-level electron depends on the wave functions of the initial and final states according to Fermi's golden rule (2.2).

$$\mu(E) \propto |\langle\psi_i|\hat{e}r|\psi_f\rangle|^2 \, \delta(E_f - E_i - h\nu) \tag{2.2}$$

The energy of a photo-electron is a function of the difference between the energy of the photon $h\nu$ and the binding energy E_0 (2.4). From the de Broglie relation (2.3) the wave vector k of a photo-electron wave is given by (2.4).

$$\lambda \ = \frac{h}{p} \tag{2.3}$$

$$k = \frac{1}{\hbar}\sqrt{2m_e(h\nu - E_0)} \tag{2.4}$$

When the photon energy reaches the binding energy (E_0) of a core electron, $\mu(E)$ increases sharply and an absorption edge appears in the spectrum. Absorption edges are named after the shell of the initial state and their energy. For example, the L_{III} edge is the transition of a 2p 3/2 state, an electron with the highest energy of the second shell.

For an isolated atom, the spectrum has a sharp step at the core-level electron binding energy and is a smooth function of energy above the edge. When the absorbing atom is placed into condensed matter, the leaving photo-electron wave scatters off surrounding atoms and produces a backscattered wave. Thus, the final state $|\psi_f\rangle$ consists of the interference of the outgoing and backscattered wave.

$$\psi_f = \psi_{outgoing} + \psi_{backscattered} \tag{2.5}$$

As a consequence, $\mu(E)$ exhibits a fine structure that extends to several hundreds of eV above the absorption edge. The interference pattern depends on the photo-electon energy, the path length of both waves (inter-atomic distance) and the phase shift caused by the scattering event. Since scattering

properties are a function of the atomic number, also the type of neighboring atoms can be determined. The modulation of the absorption (eqation 2.6) is given by $\mu_0(E)$, the absorption coefficient of the free atom and $\chi(k)$, which is referred to as the XAFS function. The XAFS represents the sum of all scattering contributions and is extracted from the absorption spectrum by background removal. For better visualization the damping of the signal is compensated by weighting, i.e. multiplication by k^n.

$$\mu(E) = \mu_0[1 + \chi] \tag{2.6}$$

The Absorption coefficient $\mu(E)$ can be measured directly in transmission mode and indirectly by fluorescence detection. For data analysis and inter-

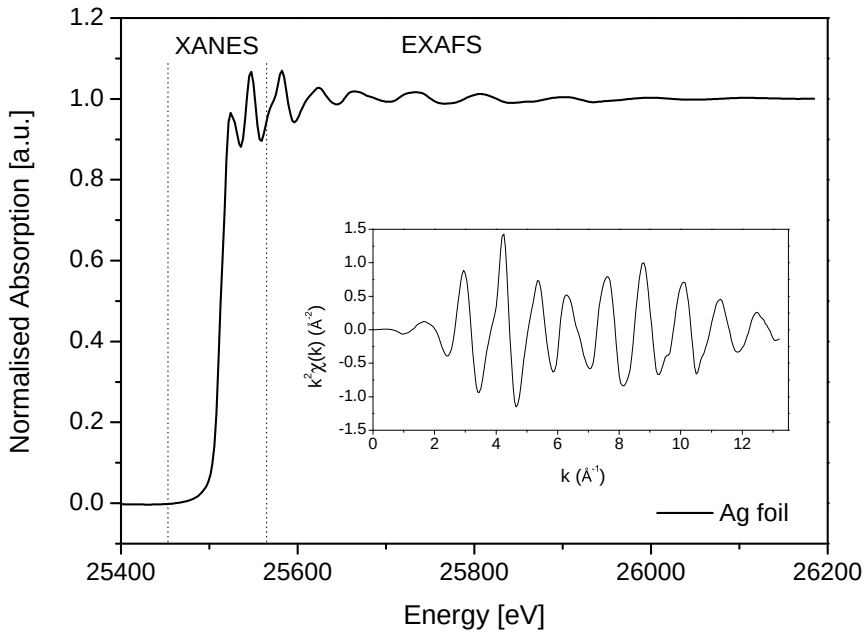

Figure 2.2. The normalised XAFS spectrum of a Ag foil and the corresponding EXAFS signal (Insert; k-weight 2).

pretation XAFS spectra are conventionally divided into two regimes, the X-ray absorption near edge structure (XANES) and the extended X-ray absorption fine structure (EXAFS). The XANES is obtained from the absorption spectrum by removal of the parabolic pre-edge background ($\mu(E) \approx E^{-3}$) and normalization to an edge-step of 1.

The EXAFS is subsequently extracted by subtracting a spline approximation of the atomic background μ_0 (equation 2.6). It must be mentioned that the basic phenomena are the same for both regimes, however some complications seem to be more pronounced in the XANES region.

2.3.2 X-Ray Absorption Near Edge Structure

The X-ray absorption near edge structure (XANES) region comprises the spectral features until about 50 eV above the absorption edge. In the pre-edge and XANES region, the final state wave function can be approximated by molecular orbitals and dipole selection rules can be applied in the qualitative interpretation of spectra although scattering effects prevail. Compared to EXAFS, XANES give a bigger signal and useful spectra can be obtained under difficult sample conditions such as very low concentrations.

The XANES region is sensitive to bond length and the symmetry of coordination, orbital occupancy and the formal oxidation state of the absorbing atom. The evaluation of XANES spectra focuses on shifts of the edge position and on the intensity of the first absorption maximum, the so-called white line. Spectra are evaluated by comparison to spectra of well-defined reference compounds and simply used as fingerprint for phases and oxidation state. The performance of linear combination fits with reference spectra is a common method to evaluate data, particularly in time-resolved measurements. For example, reduction rates can be determined with this technique. The accurate theoretical description and calculation of XANES are still active fields of research.

2.3.3 Extended X-Ray Absorption Fine Structure

The extended X-ray absorption fine structure is dependent on the local structure and can be approximated by different sine contributions. Usually, the EXAFS signal is transformed from E (eV) to k-space (Å^{-1}).
Atoms at the distance R from the absorbing atom form a coordination shell and contribute to $\chi(k)$ via so-called scattering paths j. Apart from simple backscattering, multiple scattering paths involving several atoms have to be taken into account.
The XAFS is proportional to the amplitude of the backscattered photoelectron at the absorbing atom. Its amplitude A_j is reduced by correction terms. The argument of the sine can be imagined as the time the photoelectron travels between absorber and scatterer and back. The phase shift accounts for the atom-specific scattering potential that influences the speed

of the photo-electron during this process. In the following a qualitative interpretation of the XAFS equation is given.

$$\chi(k) = \sum_j A_j \sin[2kR_j + \phi_j(k)] \tag{2.7}$$

$$A_j(k) = \frac{N_j}{kR_j^2} S_0^2 F_j(k) e^{-2k^2\sigma_j^2} e^{\frac{-2R_j}{\lambda k}} \tag{2.8}$$

j ... scattering path.
A_j ... amplitude of the backscattered photo-electron wave.
R ... inter-atomic distance.
$\phi_j(k)$ ... phase shift.
N ... coordination number. The number of a type of atoms in a coordination shell.
$F_j(k)$ ... backscattering amplitude. This element specific photo-electron property is obtained from theoretical calculations. The scattering at bound electrons is resonant in nature which means that the electron wave is enhanced when the orbital energy of the bound electron equals the scattered electron's energy.
S_0^2 ... passive electron factor. S_0^2 represents many-body effects (shake-up and shake-off) in relaxation processes after the generation of a core-electron hole. S_0^2 makes the evaluation of XAFS amplitudes (and thus the determination of N) less accurate than phases (and thus the determination of R).
σ_j^2 ... Debye-Waller factor. It describes deviations due to thermal motion or structural disorder and is defined as the root mean square deviation of R.
λ ...the mean free path of the photo-electron. A mean free path of about 25 Å and the R^{-2} terms make XAFS a local probe. λ accounts for the finite lifetime of the excited state.

EXAFS Data Evaluation

Different distances R contribute to the signal with different periodicity. To separate the sine contributions of different shells, the signal is Fourier transformed to R-space (Å). The magnitude of the Fourier transform (FT) is a radial distribution function representing the probability of finding an atom at the distance R (equation 2.9) is obtained. In order to amplify high or low Z scatterers, $\chi(k)$ is multiplied by k^n using different k-weightings (usually $n \in [0, 3]$).

$$FT(R) = \frac{1}{\sqrt{2\pi}} \int_{k_{min}}^{k_{max}} k^n \chi(k) e^{i2kR} dk \tag{2.9}$$

The goal of EXAFS analysis is to retrieve coordination numbers, distances and the Debye-Waller factors of each coordination shell. This is done by

adapting the parameters of a theoretical model calculated from an initial guess of the structure to the experimental data by a nonlinear least-squares fitting algorithm that minimizes χ^2. The noise in the data is described by ϵ .

The number of parameters that can be determined is limited statistically. The goodness of fit χ^2_{red} takes into account the degrees of freedom based on the number of independent points in the data range and the number of parameters that are refined.

$$\chi^2 = \frac{1}{\epsilon}\sum_i [\chi_i(k^n)^{data} - \chi_i(k^n)^{model}]^2 \tag{2.10}$$

$$\chi(k^n)^{model} = \chi(k^n, N, R, \sigma, \Delta E_0) \tag{2.11}$$

The path parameters (equation 2.11) are not directly adjusted in the fit, but they are written as mathematical expressions of generalized variables, which makes it possible to share variables through different paths and data sets. Generalized variables facilitate the introduction of constraints in the model, i.e. to use "'prior knowledge"' and construct a simple physical model. An example for such a constraint is the model of a mixed first shell (see 3.4.3). Fitting is preferentially done in R-space. The quality of fit is given by the χ^2_{red} or R-Factor. Recommended values for a good fit are $\chi^2_{red} < 10$ and $R < 0.05$ respectively.

2.3.4 EXAFS Analysis of Bimetallic Nanoparticles

The internal structure, i.e. the extent of alloy formation of bimetallic nanoparticles composed of two metals A and B can be elucidated by the determination of the nearest neighbor-coordination numbers A-A, A-B and B-B, B-A respectively. A model based on two quantitative parameters J_A and J_B has been described by Hwang et al. [44]. The corresponding parameters of model structures are included in figure 2.3.

$$P_{observed} = \frac{N_{A-B}}{\sum N_{A-i}} \tag{2.12}$$

$$R_{observed} = \frac{N_{B-A}}{\sum N_{B-i}} \tag{2.13}$$

$$P_{random} = x_B \tag{2.14}$$

$$R_{random} = x_A = 1 - x_B \tag{2.15}$$

$$J_A = \frac{P_{observed}}{P_{random}} \times 100\% \qquad (2.16) \qquad J_B = \frac{R_{observed}}{R_{random}} \times 100\% \qquad (2.17)$$

$\sum N_{Y-i}$ ... total number of nearest neighbors around the absorbing atom Y
x_Y ... molar fraction of atom Y

For the first coordination shell, only single scattering photo-electron contributions are important and thus two scattering paths A-B and A-A are sufficient to determine the type and number of nearest neighbors.

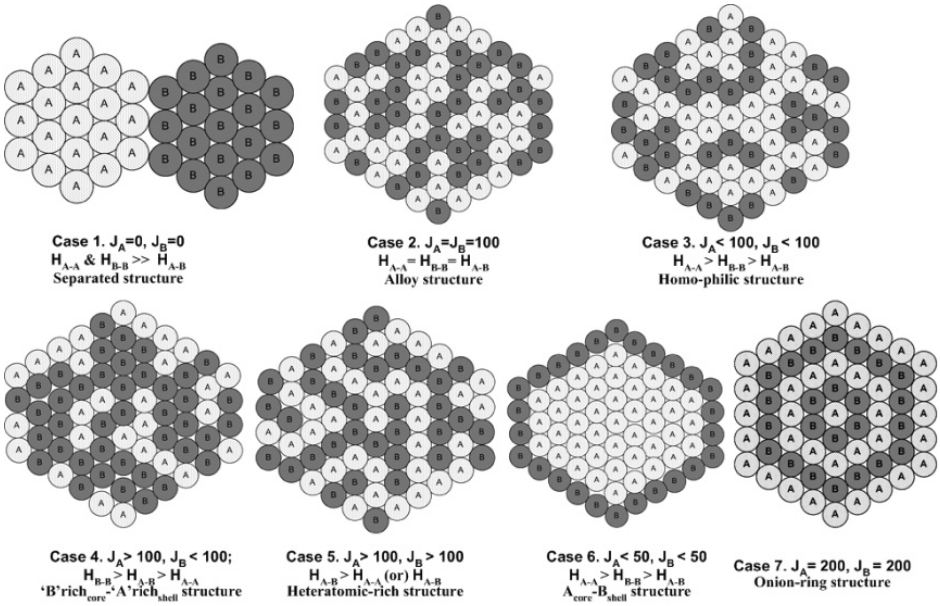

Figure 2.3. Internal structures of bimetallic nano-particles, structural parameters J_A and J_B and extent of homo- and heteroatomic interactions H_{Y-i}. Figure taken from [44].

Chapter 3

Experimental

3.1 Catalyst Preparation

Chemicals

TiO_2 P25 Degussa, 70 % anatase and 30 % rutile, $\geq$ 99.5 %, primary particle size 21 nm, nonporous, BET surface area[1] 47.5 m^2g^{-1}. TiO_2 was dried at 100 °C for at least 24 hours prior to use; $HAuCl_4 \cdot 3\,H_2O$ ABCR GmbH&Co KG, $\geq$ 99.99 % (metal based); $AgNO_3$ Fluka p.a. $\geq$ 99.5 %; urea Merck, p.a., $\geq$ 99.5 %; ZrO_2 was prepared by calcination of $Zr(OH)_4$ in air (ramp 2 °C/min and 700 °C overnight), BET surface area[1] 24.9 m^2g^{-1}, monoclinic.

The preparation of the catalyst was carried out in two steps: First, gold was deposited on the support by deposition-precipitation with urea. In the second step, a fraction of the sample was modified by the addition of Ag via incipient wetness impregnation with an aqueous solution of $AgNO_3$. The metals are deposited as Au(III) and Ag(I) species.
In a different approach, the order of preparation steps was reversed. $AgNO_3$ was deposited first, then the sample was reduced by hydrogen before the deposition-precipitation of Au(III). An overview of all samples is given in table 3.1. A summary of all samples is given in table 3.1.

3.1.1 Deposition-Precipitation

At 80 °C, $HAuCl_4 \cdot 3\,H_2O$ and urea were added to 1000 mL of deionized water to achieve a concentration of 0.84 M urea and 2.031 (1.015) mM Au(III). When the urea was completely dissolved 10.00 g TiO_2 were added and the reaction mixture was stirred vigorously for 4 h. In the course of the reaction, the pH changes from acidic to basic and an orange precipitate is deposited on the support material. The flask was covered with an aluminium foil because

[1] N_2 Physisorption, Micromeritics ASAP 2020

Sample	Au loading [wt%]	Au/Ag ratio or Ag loading [wt%]	Preparation
TiO_2 Au(2)	2	1/0	DP
TiO_2 Au(2)Ag	2	4/1	DP-IWI
TiO_2 Au(4)	4	1/0	DP
TiO_2 Au(4)Ag	4	4/1	DP-IWI
TiO_2 Ag(2)	0	2 wt%	IWI
TiO_2 Ag(0.27)	0	0.27 wt%	IWI
TiO_2 AgAu(2)	2	4/1	IWI-R-DP
ZrO_2 Ag(0.27)	0	0.27 wt%	IWI
ZrO_2 AgAu(2)	2	4/1	IWI-R-DP

Table 3.1. Samples and preparation by deposition-precipitation (DP), incipient wetness impregnation (IWI) and reduction (R) (in a fused quartz U tube; in a flow of H_2 heating ramp 10°C/min and 150°C for 60 min).

precursors and the product are light sensitive. The solid was separated by centrifugation (4000 rpm) and washed 5 times with distilled water. The product was dried under vacuum at 100 °C for one hour.

3.1.2 Incipient Wetness Impregnation

The bimetallic samples were prepared from the TiO_2 Au(2) and TiO_2 Au(4) samples by incipient wetness impregnation with a solution of $AgNO_3$. After impregnation, the sample was dried and stored in an exsiccator. For all bimetallic catalysts, the ratio Au/Ag was 4:1 which corresponds to 20 mol% Ag of the total metal loading.

The TiO_2 and ZrO_2 AgAu(2) samples were prepared as follows: Prior to deposition-precipitation of Au, Ag was deposited on the catalyst support by incipient wetness impregnation. The product was dried at 100°C in an oven, reduced at 150 °C in H_2 and subsequently Au was deposited by deposition-precipitation.
In all samples, Cl^- was not detected with Ag^+ in the washing solution of the last washing step after DP.

Storage

The catalyst precursors are sensitive to light and were stored in an exsiccator in a refrigerator. In its oxidised form, the catalyst can be stored over a long period without alteration caused by sintering of metal particles. Reduction was performed in situ directly before use.

3.2 Kinetic Measurements

Catalyst activity and selectivity were studied using a continuous fixed bed reactor: the sample is placed between two glass wool plugs in a fused quartz glass tube with an inner diameter of 4 mm. The reactor inlet is connected to a gas and vapor dosing system consisting of mass flow controllers and a saturator with a thermostat. A scheme is given in figure 3.1.

The temperature in the reactor is measured with a type K thermocouple

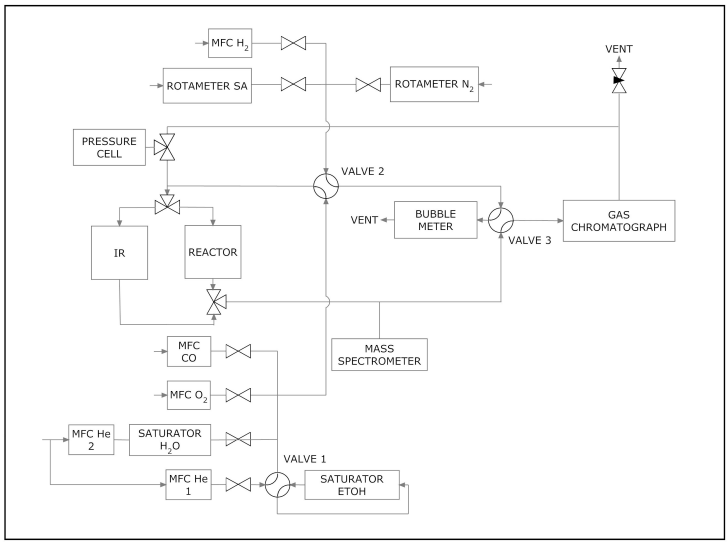

Figure 3.1. Scheme of the experimental setup that was used for kinetic measurements.

inside the reactor. The reactor temperature can be regulated via a Eurotherm 902 controller and an oven.
He was used as carrier gas. The ethanol feed was obtained by flowing He through a saturator kept at 22 °C. At 22 °C the ethanol vapor pressure is 6.638 kPa [45]. All tubes were heated by electric heating bands to avoid condensation.

Reaction products were monitored online with a Pfeiffer Vakuum Prisma Plus quadrupol mass spectrometer and a HP 6890 gas chromatograph equipped with a 6-way injection valve, two manual injection ports, a HP Poraplot Q fused silica PLOT column, a FID and a TCD detector.

The temperature programme of the GC oven consisted of 3 sections: 50 °C for 4 minutes, heating to 175 °C at 20 K/min and holding for the residual time of the 12.5 min run. Injection intervals amounted to 18 minutes approximately. The GC FID signal of ethanol was calibrated by setting different

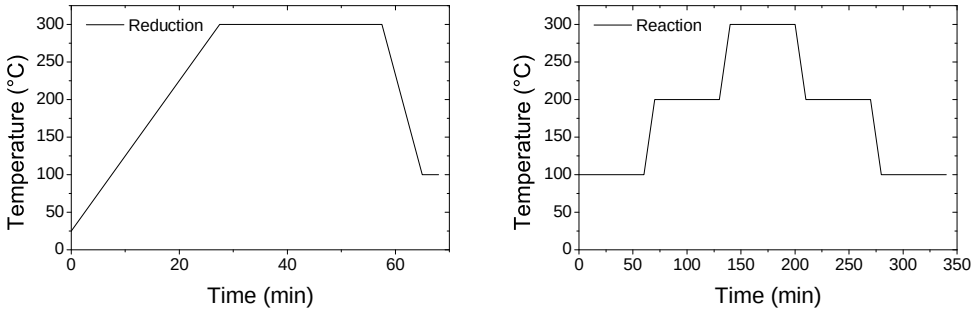

Figure 3.2. Temperature programs that were run during kinetic measurements.

saturator temperatures. The response factor of acetaldehyde was determined by manual injections of an ethanol/acetaldehyde mixture.

A mixture of 50 mg sample and an equal amount of quartz sand was used in all experiments. Catalyst reduction was carried out in a 10 mL/min flow of H_2. As illustrated by figure 3.2, the temperature program for reduction consisted of a 10 °C/min ramp and 30 min at 300 °C; after cooling down in H_2 to 100 °C the reactor was purged with He and subsequently, the reaction was carried out at various temperatures. Reaction conditions are given in table 3.2. Heating and cooling rates were 20 °C/min. At the beginning of measurements at 100 °C the total pressure at the reactor inlet was 1.13 to 1.30 bar and it increased by 0.04 to 0.2 bar during the experiments.

Experiment ($EtOH/O_2$ ratio)	Total Flow [mL/min]	Flow EtOH(g) [mL/min]	Flow O_2 [mL/min]	Flow H_2 [mL/min]
Reduction	10	0	0	10
Reaction (1/1)	67.86	3.93	3.93	0
Reaction (1/0)	63.93	3.93	0	0

Table 3.2. Conditions during reduction and reaction in kinetic measurements. He was used as carrier gas.

3.3 Transmission Electron Microscopy

TEM micrographs of selected samples were recorded in collaboration with Ass.Prof. Johannes Bernardi at the University Service Center for Transmission Electron Microscopy (USTEM), Vienna University of Technology. Measurements were performed with a 200 kV FEI Tecnai F20 S-Twin analytical transmission electron microscope that is equipped with a field emission source, an energy dispersive X-ray ultra thin window (EDX-UTW) Si detector and a high angle annular dark field (HAADF) detector for high Z-contrast images. Electron micrographs were recorded in Scanning Transmission Electron Microscopy (STEM), High Angle Annular Dark Field (HAADF) and High Resolution TEM (HRTEM) mode.

3.3.1 Pretreatment and Sample Preparation

An overview of samples analyzed by TEM is given in section 4.2 in table 4.4. All samples were reduced in a flow of H_2 by heating up at a rate of 10 °C/min and keeping the temperature at 300 °C for 30 min . Two different setups were used to reduce the catalysts: First, a quartz U tube with an inner diameter of 6 mm and a heating jacket was used. Second, samples were taken from the fixed bed reactor after reduction (10 mL/min H_2) and at different points of kinetic measurement experiments. The two samples that were reduced in a different setup consisting of a quartz U tube with an inner diameter of 6 *mm* were exposed to a lower H_2 flow rate. Samples were introduced into the microscope on a copper grid.

3.3.2 Evaluation

TEM micrographs were evaluated with the image processing programs Gatan Digital Micrograph and ImageJ. Particle size distributions were obtained through manual evaluation of HAADF images. Typically, 80-150 particles of each sample were analyzed.

3.4 X-Ray Absorption Spectroscopy

Figure 3.3. Image of the Swiss Light Source synchrotron facility at Paul Scherrer Institute, Villigen, Switzerland

Operando XAS measurements of the TiO_2 AuAg(4) and TiO_2 Au(4) samples at the Ag K-edge and Au L_{III} edge were carried out at the SuperXAS beamline of the Swiss Light Source synchrotron facility of the Paul Scherrer Institute in Villigen, Switzerland. The main features of this beamline are: energy range 4.5 - 35 keV; flux on the sample 110^{12} ph/s/400 mA; spot size on sample 100 x 100 μm^2 to 5 x 0.5 mm^2 and an intrinsic energy resolution (ΔE/E) of 2.0 10^{-4} for the Si(111) and 0.5 10^{-4} for the Si(311) monochromators.

Chemicals

5 Vol% H_2 5.0 in N_2 5.0; 10 Vol% O_2 5.0 in He 5.0; He 5.0; EtOH abs. p.a.

3.4.1 Experimental Setup

The catalysts were pressed into self-supporting wafers and placed in an in-situ continuous flow cell which allows performing measurements in transmission mode. The cell is equipped with an inductive heater, water cooling and Al foil windows. Three ionization chambers were used to monitor the incident and transmission intensities as well as to simultaneously perform energy calibration with a metal foil standard. A scheme of the experimental setup is

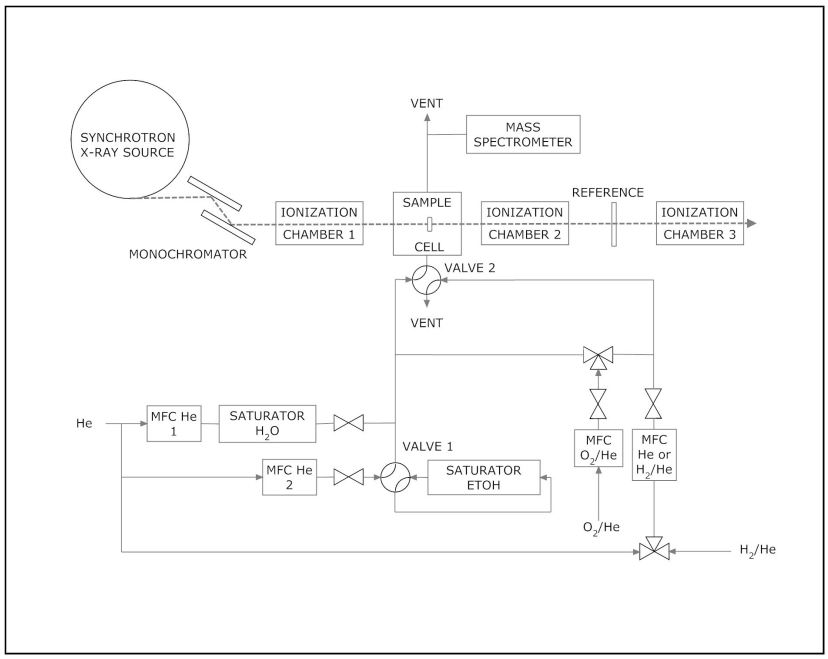

Figure 3.4. Experimental setup for XAFS measurements.

shown in figure 3.4. In transmission mode, the sample mass m_{sample} in a pellet needed to obtain an edge jump $\Delta\mu$ can be calculated from the following equations, with molar ratio x_i, tabulated [46] absorption cross sections σ_i of each element i, the pellet surface A_{pellet} at energies E below and above the threshold energy E_0.

$$A(E) = \log \frac{I_0}{I} = \frac{\sum_i x_i \sigma_i(E) \cdot m_{sample}}{A_{pellet}} \tag{3.1}$$

$$\Delta\mu = A(E_0 + 20) - A(E_0 - 20) \tag{3.2}$$

Reduction and reaction conditions are summarized in table 3.4. Temperature

Edge	Sample	Sample in pellet [mg]	Transmission (post edge) [%]	Edge step [10^{-2}]
Au L_{III}	TiO_2 Au(4)Ag	15	10	8.72
Au L_{III}	TiO_2 Au(4)	15	10	8.78
Ag K	TiO_2 Au(4)Ag	70	21	2.27

Table 3.3. Result of calculations to optimize sample mass in the pellet.

Experiment ($EtOH/O_2$ ratio)	Total Flow [mL/min]	Flow EtOH(g) [mL/min]	Flow O_2 [mL/min]	Flow H_2 [mL/min]
Reduction	40	0	0	2
Reaction (1/0)	10.16	0.16	0	0
Reaction (1/1)	11.76	0.16	0.16	0
Reaction (1/2)	13.36	0.16	0.32	0
Oxidation	16	0	1.6	0

Table 3.4. Reduction, oxidation and reaction conditions.

programs are given in figure 3.5. The EtOH vapor pressure was calculated from [45].
For each absorption edge, two pellets were used for measurements. Reduction A followed by oxidation with the first and cycles of reduction B followed by reaction under different conditions with the second pellet.

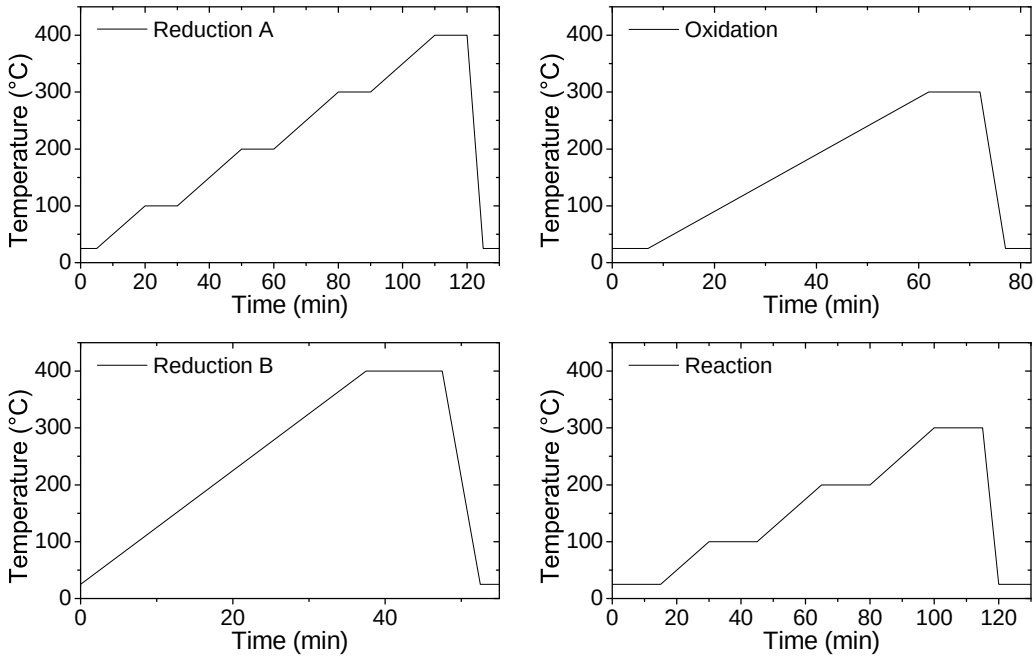

Figure 3.5. Temperature programs which were run during XAFS measurements.

3.4.2 Data Processing and Analysis

Data processing and analysis was carried out with the IFEFFIT software package including ATOMS, HEPHAESTOS, ATHENA and ARTEMIS [46]. The ATHENA software was used for data processing which includes energy calibration (the zero-crossing of the second derivation of a reference spectrum is set at the tabulated edge energy) shifting all spectra via aligning their corresponding reference spectra, merging of scans (typically 3-9) in $\mu(E)$, setting the pre-and post edge energies relative to E_0 (Ag K: -180 to -30 eV, Au L_{III}: -80 to -30 eV) as well as normalization ranges (Ag K: 50 to 650 eV, Au L_{III}: 50 to 300 eV) and spline ranges and finally setting the E_0 to a 0.5 fraction of the edge step. The Rbkg parameter for background removal was carefully adjusted in R space.

3.4.3 EXAFS Analysis: Fitting Model

Scattering Paths

Only the EXAFS of the Ag K edge was analyzed. FEFF 6.0 (based on muffin-tin potential approximation) calculations using modified ATOMS input files for Au metal were performed. Firstly, the central Au atom was substituted by Ag and a FEFF calculation was run to obtain the backscattering amplitude and phase shift for the Ag-Au scattering path. The input file was further modified by replacing the 12 Au atoms of the first coordination shell by Ag. FEFF was run with this input file to calculate the parameters of the Ag-Ag scattering path.

Determination of S_0^2

The coordination number N and the passive electron reduction factor S_0^2 are completely correlated, thus only their product can be obtained experimentally. As S_0^2 is atom specific and chemically transferable, its value can be obtained from a well known reference compound. $S_0^2 = 0.9563310$ was obtained from a first shell fit of Ag foil data (N=12, amp as "'guess"' variable, k-weight 2, R range 1.4 to 3). For a k-weight of 1 and 2 a value of 0.9412 was determined.

Determination of Ag-Au and Ag-Ag Coordination Numbers

Only single scattering photo-electron contributions are important for the first coordination shell, and thus two scattering paths A-B and A-A can be used to determine the number of nearest neighbors. Parameters and variables

used for fitting Ag-Ag and Ag-Au paths are listed in table 3.5. For Au/TiO_2 with an average particle size of 2.1 nm, an average coordination number of 10 was determined [4, 47]. This information can be used to restrain the total CN. The Ag and Au coordination numbers are obtained by simultaneously fitting two scattering paths that are weighted by a scaling factor x. Seven parameters (see table 3.5) are refined in this mixed first shell model; A k-range of 2 to 11.29 $Å^{-1}$, R range of 1.4 to 3.2 Å and a k-weight of 2 were used in the fits.

The mixed first shell model was also applied to fit the Ag foil spectrum. Based on FEFF-calculations using the Ag lattice parameter and N =12 a value of x = 98,7 ± 3.2 % is obtained. Based on FEFF-calculations using the Au lattice constant the fit yields x = 90.9 ± 5.7 %.

Path	Parameter	Type	Variable Name	Expression	(Initial) Value
Ag-Au	N			1	1
Ag-Au	S_0^2			amp×Au	
Ag-Au	$delE_0$	guess	enot	enot	0
Ag-Au	delR	guess	delr	delr	0
Ag-Au	σ^2	guess	ss	ss	0.003
Ag-Au	amp	set	amp		0.9563310
Ag-Au	Au	guess			10
Ag-Au	N			10	10
Ag-Au	S_0^2			amp×$(1-x)$	
Ag-Au	$delE_0$	guess	enot	enot	0
Ag-Au	delR	guess	delr	delr	0
Ag-Au	σ^2	guess	ss	ss	0.003
Ag-Ag	N			10	10
Ag-Ag	S_0^2			amp×x	
Ag-Ag	$delE_0$	guess	enot_1	enot_1	0
Ag-Ag	delR	guess	delr_1	delr_1	0
Ag-Ag	σ^2	guess	ss_1	ss_1	0.003
Ag-i	amp	set	amp		0.9563310
Ag-i	x	guess	x		0.2

Table 3.5. Fit parameters and variables. top: Ag-Au single path; bottom: mixed first shell model.

3.5 Infrared Spectroscopy

In situ transmission FTIR measurements of CO adsorption were carried out on a Bruker Vertex 70 spectrometer with a resolution of 4 cm^{-1}. The instrument is constantly purged with dry air and equipped with a globar light source and a mercury cadmium telluride (MCT) detector.

Typically, 120 scans were added to a spectrum to achieve a good signal/noise ratio.

3.5.1 In Situ Vacuum Cell

The in situ FTIR vacuum cell is equipped with CaF_2 windows. A pressure of approximately 10^{-6} mbar can be reached with a rotary vane pump and a Pfeiffer Vakuum turbomolecular pump. A pellet of the sample is prepared and introduced into the cell in a sample holder that is equipped with a heating wire and a type K NiCr/NiAl Thermocoax Company thermocouple that are connected to a Eurotherm 902 temperature controller. The sample can be cooled via a cooling loop in the sample holder. Gases and vapors can be introduced via a leak valve. The pressure in the chamber is monitored by two pressure gauges, a MKS Baratron type 626 pressure gauge for pressures above 1mbar and by a Pfeiffer Vakuum CMR 264 compact capacitance gauge for pressures below 1mbar. Pretreatment and measurements can be performed in a wide range of conditions. (77 to 800 K).

It must be mentioned that intensities of absorption peaks are hardly comparable when different pellets are used. In addition, the temperature in the pellet may deviate from the temperature measured on the sample holder.

3.5.2 Pretreatment and Experimental Procedure

After mounting the sample, temperature programmed reduction with a final temperatur of 400 °C (reduction A, see figure 3.5) in 5 % H_2 in N_2 at 900 mbar was performed. After cooling down to room temperature, the cell was evacuated and cooled below -115 °C by purging the cooling loop with liquid nitrogen. Subsequently 5 mbar CO were introduced. Cooling was stopped and spectra were taken as the temperature increased; finally 80 °C were reached by heating up at a rate of 5 °C/min.

Chapter 4

Results and Discussion

4.1 Kinetic Measurements

Kinetic measurements were performed in order to study the activity and selectivity of the catalysts. Measurements of ethanol oxidation were carried out using 50 mg catalyst, an ethanol/O_2 ratio of 1/1. On selected samples, the dehydrogenation reaction was carried out at the absence of O_2.

4.1.1 Ethanol Conversion

Ethanol conversion as a function of time on stream and temperature is given in figure 4.1. When the reaction mixture is admitted to the freshly reduced catalyst at 100 °C, conversions are below 5 %. At 200 °C the activity of the bimetallic Au(2)Ag catalysts is higher than the activity of the monometallic Au and Ag catalysts. The difference between the monometallic and bimetallic catalysts amounts to approximately the conversion of the monometallic Ag catalyst.

When Ag is deposited first on TiO_2 (TiO_2 AgAu(2)) a higher ethanol conversion was measured. The highest conversion rate was observed over ZrO_2 supported catalysts. Interestingly, the monometallic ZrO_2 Ag(0.27) catalyst outperformed the bimetallic ZrO_2 AgAu(2) catalyst.

4.1.2 Reaction Products and Selectivity

Acetaldehyde is the main product; the main side product is ethyl acetate followed by CO or CO_2. Moreover diethylether could be identified among up to 10 peaks of reaction products in the FID signal. H_2 was detected by MS as it can not be detected by FID and TCD using He as carrier gas.

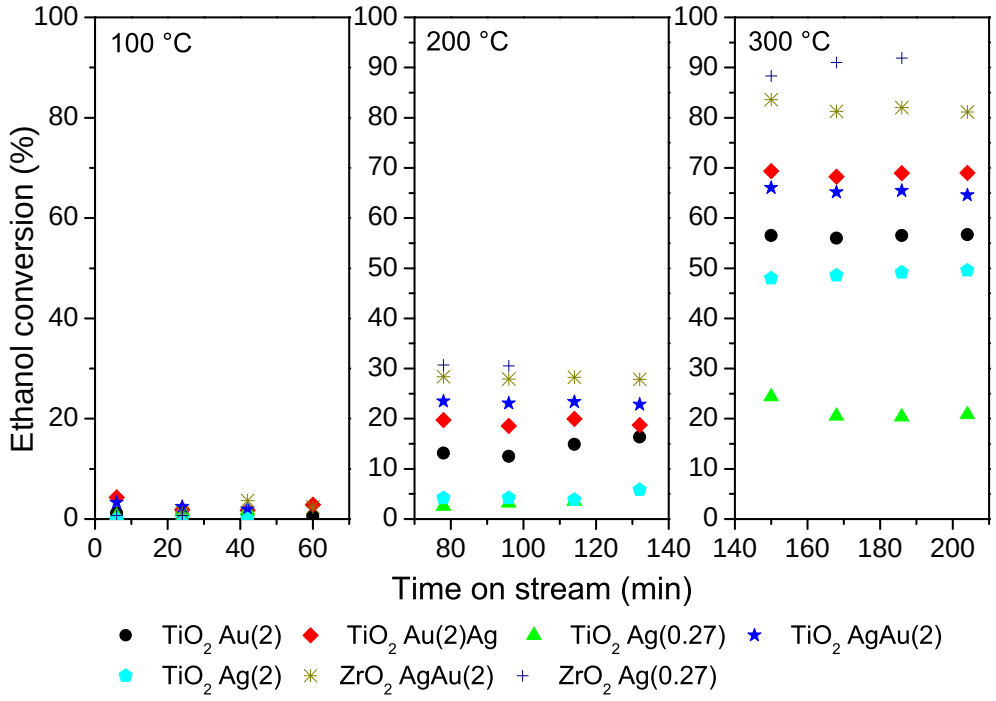

Figure 4.1. Conversions at 100, 200 and 300 °C and an ethanol/O_2 ratio of 1/1.

Catalyst	200 °C	300 °C	200 °C
TiO_2 Au(2)	97	92	94
TiO_2 Au(2)Ag	97	92	98
TiO_2 Ag(0.27)	93	94	98
TiO_2 AgAu(2)	90	90	93
ZrO_2 AgAu(2)	93	84	95
ZrO_2 Ag(0.27)	96	97	97

Table 4.1. Selectvities to acetaldehyde (% FID peak areas) when the reaction was carried out at an ethanol/O_2 ratio of 1/1 at 100, 200, 300 and 200 °C.

As some side products could not be identified, selectivities can only be estimated. In table 4.1 an estimation of selectivities to acetaldehyde based on GC peak areas (assuming a uniform response factor for all products) are given. Generally, selectivities are very high and especially good values were obtained at 200 °C after performing the reaction at 300 °C. Except for the monometallic TiO_2 Au(2) catalyst an increase in selectivity was observed at 200 °C after performing the reaction at 300 °C. At 300 °C, selectivities were lower but still above 90 % for all samples. The TiO_2 AgAu(2) catalyst

exhibits the lowest selectivity. It can be concluded that adding Au first leads to more selective TiO_2 catalysts. Interestingly, at 300 °C the ZrO_2 Ag(0.27) catalyst exhibited the highest conversion and selectivity.

4.1.3 Deactivation

As evident from figure 4.2 performing the reaction at 300 °C leads to a decrease in ethanol conversion at 200 °C. The activity of monometallic Ag catalysts decreased dramatically and the difference between TiO_2 AgAu(2) and the monometallic TiO_2 Au(2) catalysts disappeared. At 100 °C at the end of measurements no catalytic activity was observed. The TiO_2 Au(2)Ag

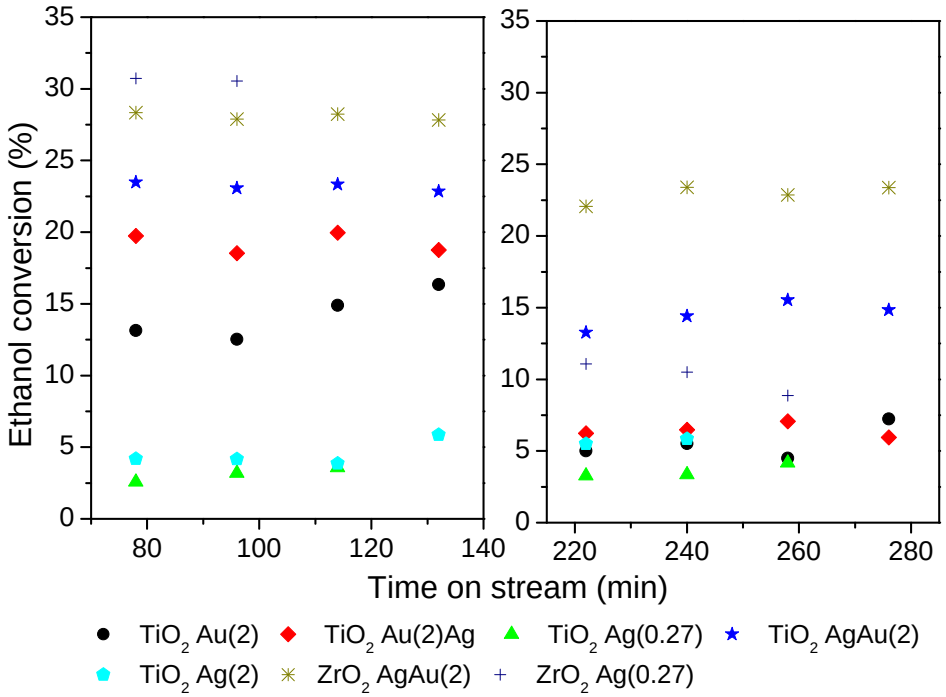

Figure 4.2. Comparison of ethanol conversion at 200 °C before (left) and after (right) performing the reaction at 300 °C. The ethanol/O_2 ratio was 1/1.

and TiO_2 AgAu(2) catalysts could not be reactivated by repeating the reduction procedure. No significant increase of ethanol conversion or change in selectivity was observed at 100 and 200 °C. This suggests an irreversible deactivation mechanism that could be related to morphological changes of the metal particles. In TEM measurements (see section 4.2) of the used catalyst no indication of increased particle size was found, which rather excludes sintering.

4.1.4 Ethanol Dehydrogenation

Unlike oxidation, ethanol dehydrogenation is an endothermic reaction and product formation is favoured at higher temperatures. The difference in the thermodynamic equilibrium must be considered when kinetic data of these reactions are compared. Ethanol dehydrogenation was carried out at 200 °C by turning off the O_2 feed at the end of ethanol oxidation experiments (as described in section 3.2). Conversions and selectivities are given in table 4.2.

Ethanol dehydrogenation using 4 wt% Au TiO_2 catalysts was performed

Catalyst	Ethanol conversion (%)	Selectivity (%)
TiO_2 Au(2)	2	97
TiO_2 Au(2)Ag	1	90

Table 4.2. Ethanol conversion and Selectivities to acetaldehyde (% FID peak areas) of the dehydrogenation reaction at 200°C.

after exposure to oxidation reaction conditions at 200 °C. Ethanol dehydrogenation yielded substantially lower ethanol conversion and selectivities to acetaldehyde. The bimetallic catalysts exhibited lower reaction rates than the monometallic catalysts.

Catalyst	Ethanol conversion (%)	Selectivity (%)
TiO_2 Au(4)	30	85
TiO_2 Au(4)Ag	22	88

Table 4.3. Ethanol conversion and selectivities to acetaldehyde (% FID peak areas) of the dehydrogenation reaction at 250°C. After reduction pretreatment the catalysts were exposed to oxidation reaction conditions at 200 °C.

4.1.5 Accuracy and Reproducibility

At the conditions given in table 3.2, the ethanol feed is poorly reproducible and deviates by more than 10 % [48] in some cases. The standard deviation of the TCD O_2 peak area was 1.75 %. Very likely, ethanol condensed at cold spots in the equipment. Therefore, further measurements at lower reactant concentrations (lower saturator temperatures and replacing a 50 mL/min O_2 mass flow controller by a smaller one) appear to be beneficial for accurate results.

4.2 Transmission Electron Microscopy

In this section, results of TEM investigations of TiO_2 and ZrO_2 supported Au and Au/Ag catalysts are presented. The aim of TEM examinations is to determine the particle size and the dispersion of the catalytically active phase. In addition, it is of great interest to measure the distribution of Au and Ag in the sample to establish a relation between the properties of the particles and catalytic performance.

As evident from figure 4.3, the metal particles are well dispersed on the TiO_2 support. In contrast, in the ZrO_2 Ag(2)Au sample metal particles are bigger and particle dispersion is not as good.

4.2.1 Distribution of Au and Ag

It is difficult to obtain detailed information on the distribution of Au and Ag in the sample: Due to very similar lattice parameters,(Au 4.07833 Å and Ag 4.08626 Å), it is not possible to distinguish between Au and Ag particles by measuring lattice parameters with HRTEM. In principle, Z-contrast should allow to distinguish between Au- and Ag-rich domains, as the latter should appear brighter in HRTEM. However, particles appear very similar. Sometimes, as can be seen in figure 4.4 darker areas within a particle were observed. This effect can be ascribed to particle shape or different distribution of Au and Ag.
Energy dispersive X-ray fluorescence spectroscopy (EDX) was employed to study the distribution of Au and Ag. The spatial resolution of this technique is limited by the volume of interaction and the detection limit of the detector. The concentration of Ag is 0.54 wt%. Interestingly, Ag was not detected even when a very large area of the sample was analyzed. In a very similar work on AuAg catalysts supported on TiO_2 prepared by deposition of Ag and then Au, Sandoval et al. [49] were able to determine the composition of single particles.

4.2.2 Particle Size

HAADF images were used to determine values of mean particle size and size distribution. As shown in figure 4.3, very few rather large particles with diameters of about 30 - 70 nm occur in all reduced samples. These particles were disregarded in the determination of the size distribution since the vast majority of particles is much smaller. In addition, catalytic properties are

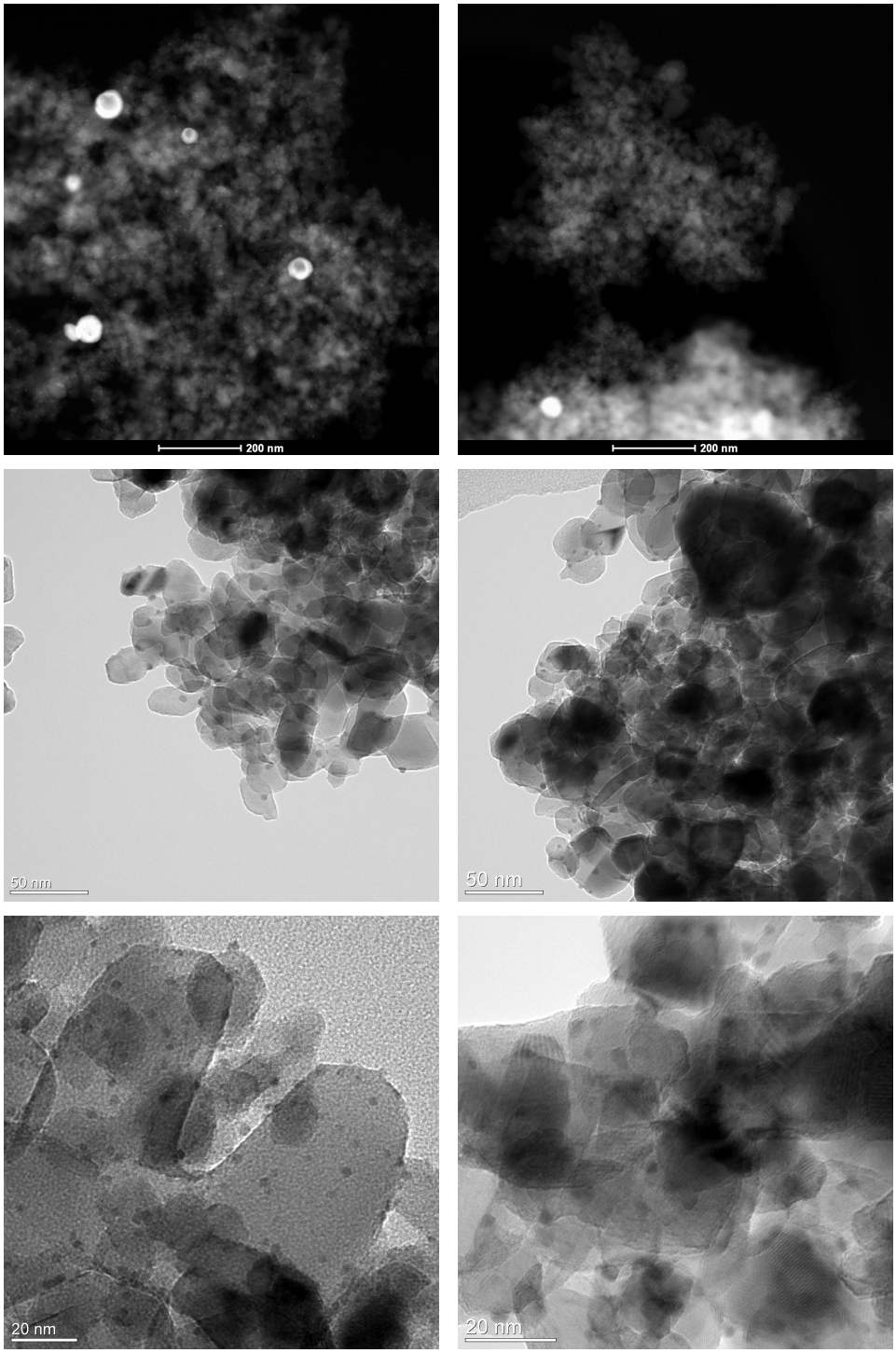

Figure 4.3. HAADF and HRTEM images of TiO_2 Au(4) (left) and TiO_2 Au(4)Ag (right) catalysts after reduction at 300 °C in a flow of H_2 in a fused quartz U tube with a heating mantle.

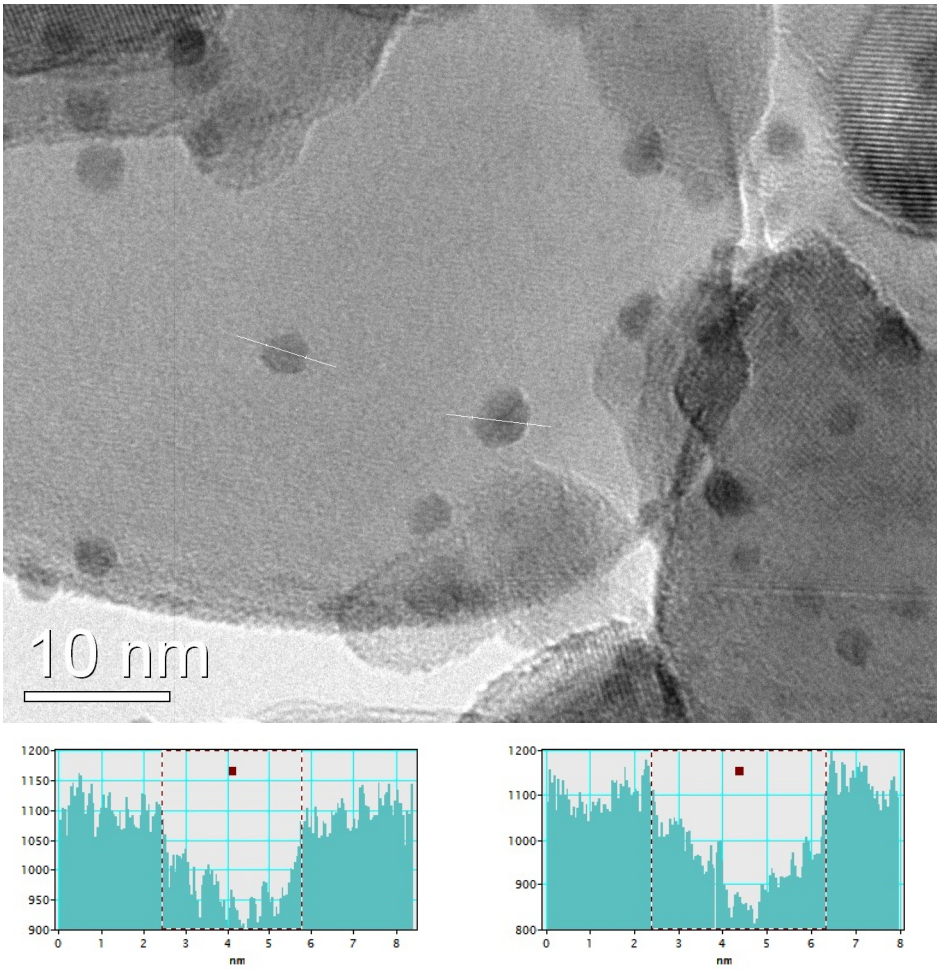

Figure 4.4. HRTEM image and intensity profiles of two particles of TiO_2 Au(4)Ag after reduction at 300 °C in a 10 mL/min flow of H_2 in the fixed bed reactor.

governed by the small particles and the contribution of the rather large particles is marginal.

The mean particle size d of the monometallic sample compares well with the result obtained for the bimetallic sample. Figure 4.5 contains HAADF images and histograms of TiO_2 Au(4) and TiO_2 Au(4)Ag. It can be concluded that the presence of Ag does not lead to significant increase in particle size; on the contrary, both a slightly lower value for d and the standard deviation was found in the sample containing Ag. Particle size clearly depends on the reduction conditions: a higher H_2 flow rate generated smaller particles. In the quartz reactor the hydrogen flow was higher than in the U tube. This effect

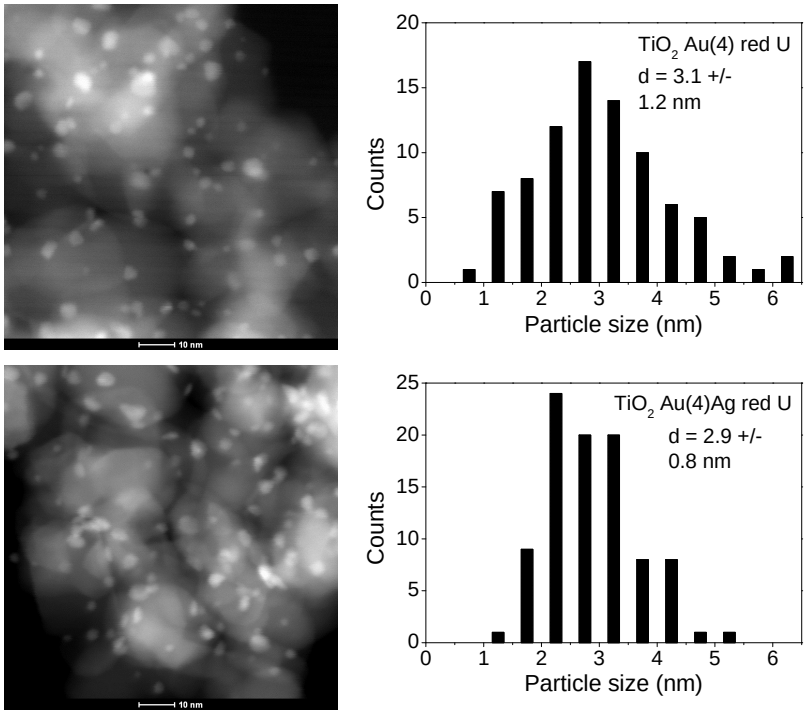

Figure 4.5. HRTEM and HAADF images of TiO_2 Au(4) (top) and TiO_2 Au(4)Ag (bottom) catalysts after reduction at 300 °C in a 10 mL/min flow of H_2 in a U tube and corresponding histograms.

was also reported by Zanella [37]. As reduction is an exothermic process, a low hydrogen flow could lead to a significant local increase of temperature enhancing the mobility of Au and thus yielding bigger particles.

From a statistical point of view, it is difficult to obtain reliable results of particle size distributions because the number of measured particles is very small. Nevertheless, representativeness can be assumed given the homogeneity of the sample: No differences were observed at different spots.

The catalyst TiO_2 Au(4)Ag was exposed to reaction conditions at 100, 150 and 200 °C; interestingly, a decrease in the mean particle size was found. Data in figure 4.6 suggests that also the TiO_2 Au(2)Ag sample exhibits comparatively small particle size upon exposure to reaction conditions at 300 °C. Redispersion of particles upon exposure to reaction conditions can not be excluded, however the change in particle size can also be explained by sintering of very small Au/Ag clusters that are not visible in HAADF before the longterm exposure to higher temperatures.

The ZrO_2 sample exhibits a broader particle size distribution compared

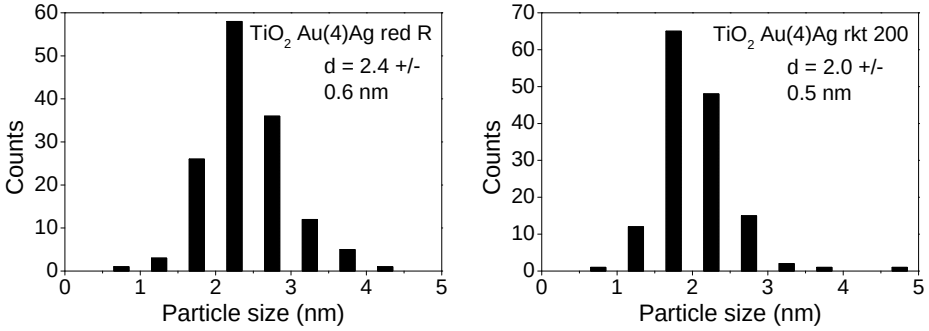

Figure 4.6. Particle size distributions of TiO_2 Au(4)Ag after reduction (left) in the reactor and after reaction at 200 °C (right).

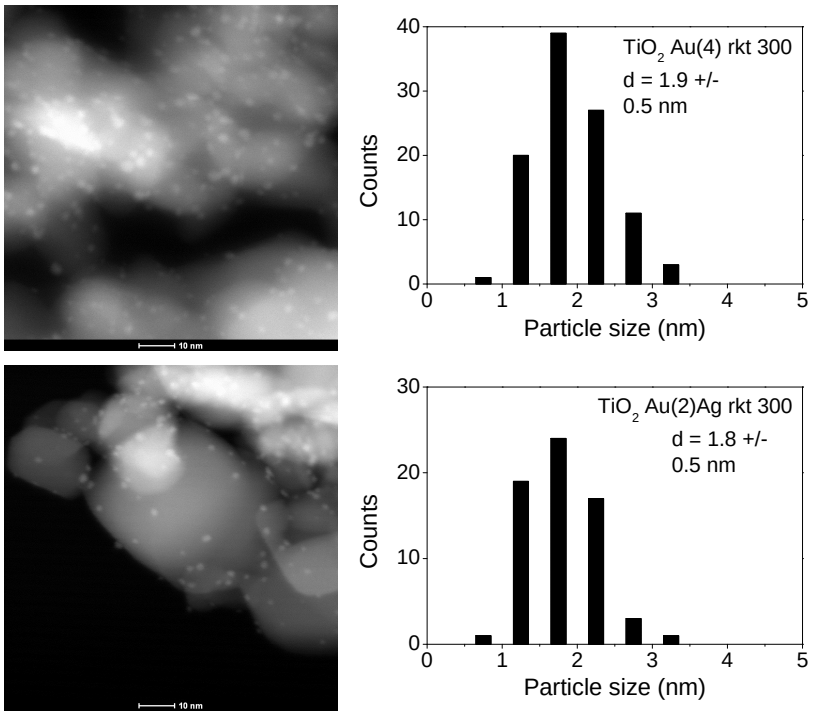

Figure 4.7. TiO_2(4)Au after cycles of reduction and reaction at 100, 200 and 300 °C (top) and TiO_2 Au(2)Ag after reaction at 300 °C (bottom).

to the TiO_2 samples. Similar to the TiO_2 samples,also a small number of rather large metal particles could be observed in addition to the large fraction of small particles. A HAADF image and the particle size distribution are given in figure 4.8.

Short descriptions of samples and particle sizes determined by TEM are given in table 4.4.

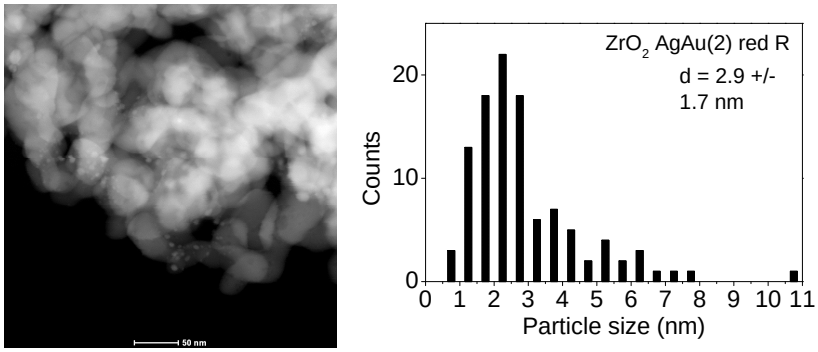

Figure 4.8. HAADF image of ZrO_2 AgAu(2) after reduction at 300 °C in a 10 mL/min flow of H_2in the reactor and particle size distribution.

Sample	Pretreatment	Particle Size (nm)
TiO_2 Au(4) red U	Reduction U tube	3.1 ± 1.2
TiO_2 Au(4)Ag red U	Reduction U tube	2.9 ± 0.8
TiO_2 Au(4) rkt 300	Alternately Red. at 300 °C and Reaction at 100, 200, 300 °C	1.9 ± 0.5
TiO_2 Au(4)Ag red R	Reduction reactor	2.4 ± 0.6
TiO_2 Au(4)Ag rkt 200	Reaction at 100, 150, 200 °C	2.0 ± 0.5
TiO_2 Au(2)Ag rkt 300	Reaction at 300 °C	1.8 ± 0.5
ZrO_2 Ag(2)Au red R	Reduction reactor	2.9 ± 1.7

Table 4.4. Overview of samples analyzed with TEM. The standard reduction treatment was 10 °C/min ramp and 30 min at 300 °C in a flow of H_2. Reaction conditions are given in section 3.2.

4.3 X-Ray Absorption Fine Structure

In this section, results of operando X-ray absorption measurements at the Ag K and Au L_{III} edges of the TiO_2 Au(4)Ag and TiO_2 Au(4) catalysts will be discussed.

4.3.1 XANES

In general, differences between the K-edge and L_{III} edge spectra originate in the dipole selection rules. At K edges, transitions from 1s to final states with p symmetry are probed whereas at the L_{III} edge transitions from 2p 3/2 to s and d final states are allowed. Transitions to d final states yield a more intense signal than transitions to s final states.

XANES of as-prepared and reduced samples

Reference spectra of metal foils and spectra taken before and after sample reduction are given in figure 4.9. It can be clearly inferred that both Au and Ag are present in an oxidised state after catalyst preparation. Different temperature programs during reduction did not lead to differences in the XANES of the reduced catalysts.

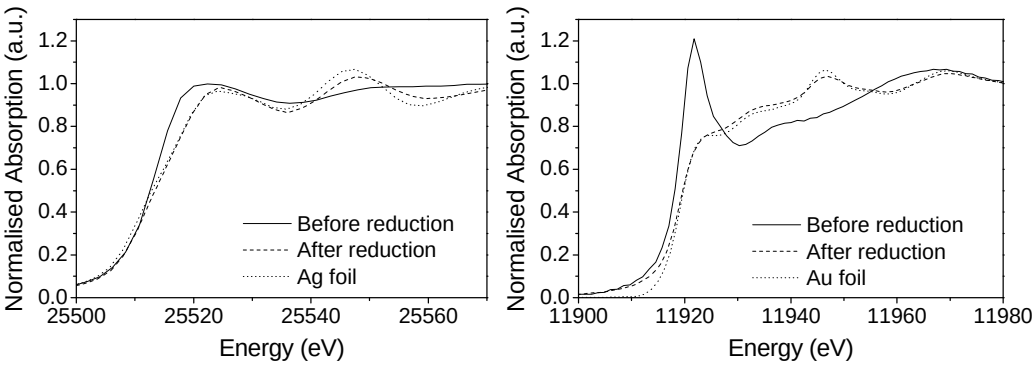

Figure 4.9. XANES of as-prepared and reduced bimetallic TiO_2 Au(4)Ag catalysts and bulk metal reference spectra. Ag K edge (left) and Au L_{III} edge spectra (right) of the catalysts were taken at 25 °C in a flow of He before reduction and in a flow of H_2 at the end of reduction A (Red A* 25 °C).

Figure 4.9 also illustrates differences between the spectra of the metal foils and the reduced sample. Absorption peaks are less pronounced in the XANES of the catalyst, which is mainly due to the small particle size and higher disorder, but it could also be brought about by alloy formation or

interactions with the support material. The Ag K-edge position of the as-prepared sample is shifted to lower energies compared to the Ag foil and the reduced sample. The oscillatory features in the Ag XAFS of the as-prepared catalyst are very weak. The Ag edge XANES absorption peaks of the reduced catalyst are clearly shifted to higher energies relative to the Ag foil.

The Au L_{III} XANES of the as-prepared catalyst exhibits a very intense and sharp white line that is typical of oxidised Au and reflects holes in the d band. The sharp white line can be explained by transitions to unoccupied and relatively well localized d-states of Au(III). Moreover, the edge position is shifted to lower energies in the XANES of oxidised Au. Upon reduction, metallic Au is formed and the d bands are filled. Thus, the white line is suppressed and the threshold energy increases.

Also in the XANES of the monometallic TiO_2 Au(4) catalyst shown in figure 4.10, absorption maxima are less pronounced compared to the bulk Au spectrum. This can be related to reduced coordination numbers and increased disorder in small particles. There is no significant difference between the Au XANES of the mono- and bimetallic catalysts.

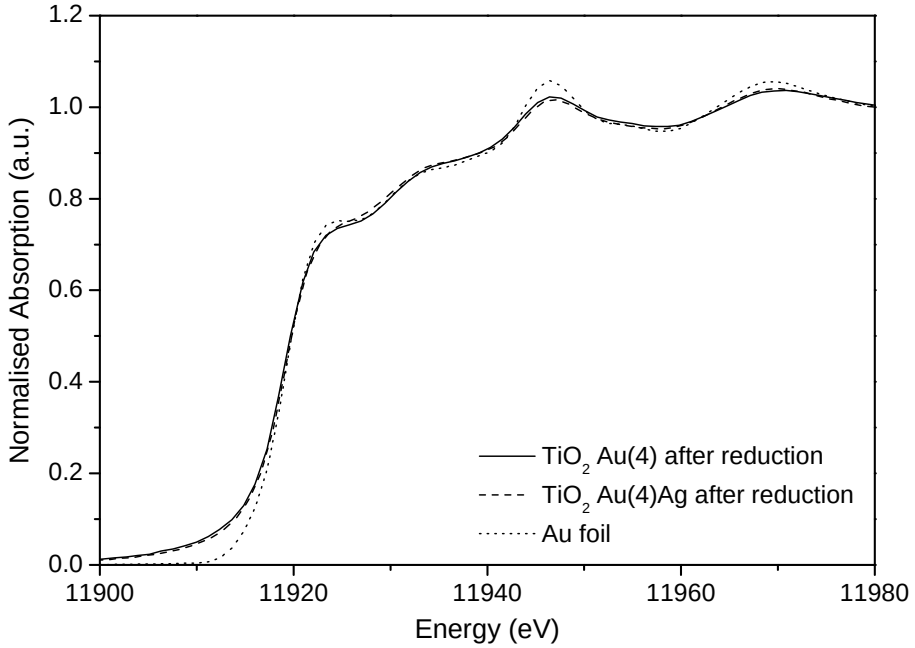

Figure 4.10. Au L_{III} XANES of TiO_2 Au(4), TiO_2 Au(4)Ag catalysts after reduction and Au foil spectrum.

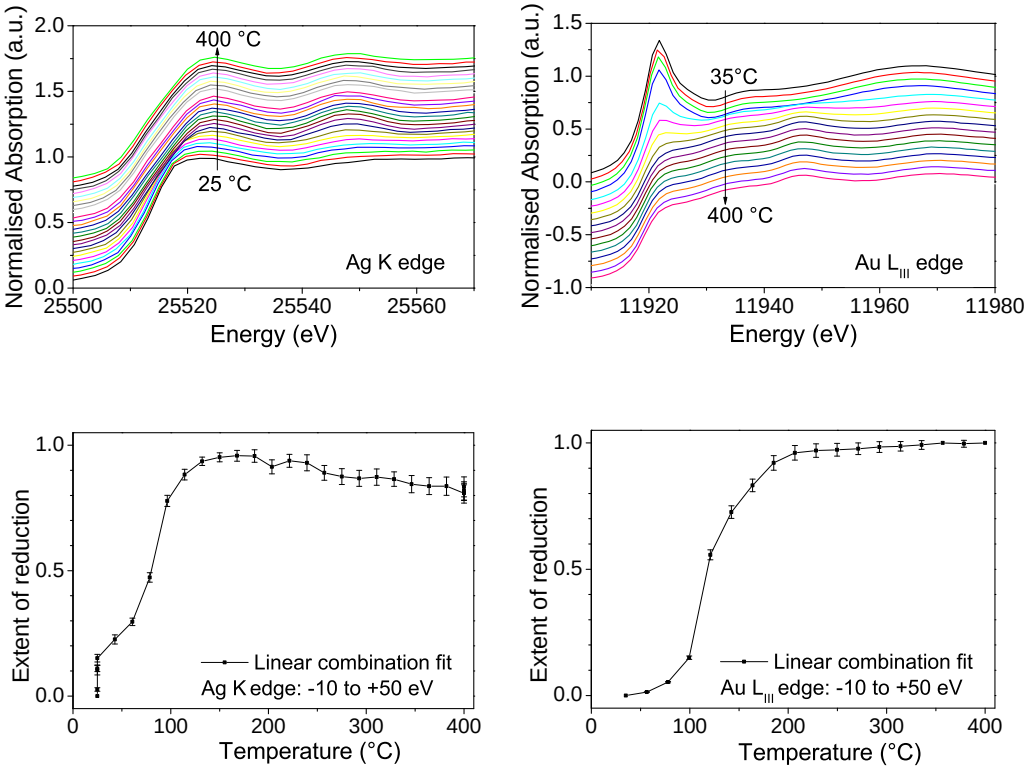

Figure 4.11. Reduction of the TiO_2Au(4)Ag catalyst. Evolution of XANES spectra and result of linear combination fits of the Ag K edge (left) and the Au L_{III} edge (right) spectra while heating up at 10 °C/min to 400 °C (reduction B) in a flow of 5 % H_2. Spectra taken at 25 °C at the beginning and at the end (Red B* 25 °C) of the experiment served as standards in the fit.

Temperature Programmed Reduction

Temperature programmed reduction of the bimetallic TiO_2Au(4)Ag catalyst was performed in a flow of H_2. The temperature was increased from 25 to 400 °C at a rate of 10 °C /min. The extent of reduction was determined by fitting each intermediate spectrum as a linear combination of the end members of the experiment. The evolution of XANES spectra and the results of the linear combination fits are given in 4.11.

The linear combination fits indicate that the reduction of Ag and Au is completed at 140 and 180 °C respectively. The formation of Au, Ag and Au/Ag clusters and particles takes place at these temperatures. The melting point and the Tamman temperature of small Au particles are substantially decreased compared to bulk gold [4].

The linear combination fits of the Ag K edge XANES (figure 4.11) suggest that the oxidation state of Ag decreases towards the end of the reduction treatment, which could be ascribed to alloy formation. However, at elevated temperatures the oscillatory features of the XAFS are increasingly damped. Thus, the similarity of the Ag K edge spectra with the oxidised standard increases. Only seemingly, the extent of reduction decreases. This effect is absent in the linear combination fits of the Au L_{III} edge XANES.

Temperature Programmed Oxidation

The freshly reduced catalyst was exposed to 10 % oxygen and heated up at 5 °C/min to 300 °C in the temperature programmed oxidation (TPO) experiment. Inspection of figure 4.12 clearly indicates that Ag is oxidised, whereas the oxidation state of Au remains unaffected. The extent of the

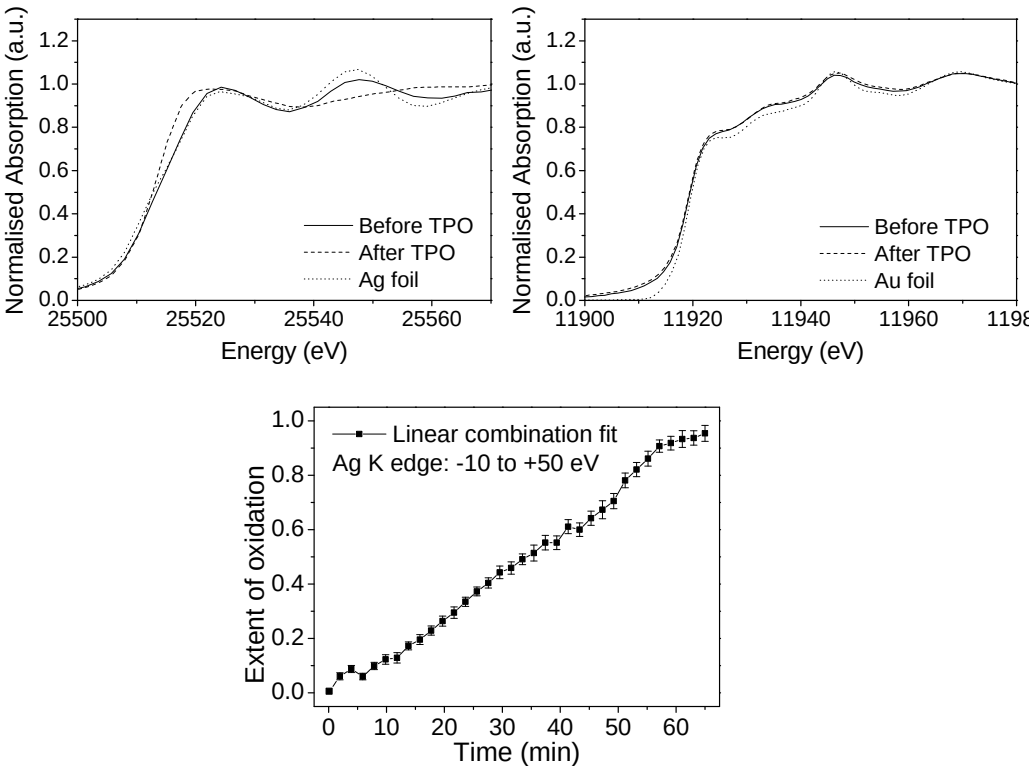

Figure 4.12. Temperature programmed oxidation (TPO) of the TiO_2 Au(4)Ag catalyst consisting of a 5 °C/min ramp and 10 min at 300 °C in a flow of 10 % O_2). The Ag K edge spectra taken at 25 °C before and after the oxidation experiment served as standards for linear combination fits.

oxidation of Ag was determined by linear combination fits with the first and last Ag K edge spectrum, each taken at room temperature, as standards. The total extent of oxidation after TPO is unknown. The Ag XANES of the oxidised catalyst is very similar to the Ag XANES of the as-prepared catalyst. Interestingly, the spectrum does not resemble the XANES of Ag_2O but is similar to AgCl [49]. Compared to reduction, oxidation is a slow process. In alloy particles segregation must take place when Ag reacts with O_2 while Au remains reduced.

Reaction

Ethanol oxidation was performed at 25, 100, 200 and 300 °C at ethanol/O_2 ratios of 1/0, 1/1 and 1/2.

In the Au L_{III} spectra acquired under these reaction conditions, no significant change is observed. This is in line with results of the temperature programmed oxidation experiment. No evidence of a change in the oxidation state of Au was found. Spectra are given in figure 1 in the appendix.

Figure 4.13 reveals the influence of the O_2 partial pressure on the Ag K edge XANES at 200 °C: The edge position is shifted towards lower energies and oscillations are less pronounced when the amounts of O_2 in the reaction mixture is increased. Comparison with the spectra of the as-prepared (figure 4.9) and oxidised sample (figure 4.12) confirms the increasingly oxidised character of Ag as the oxygen partial pressure rises.

Figure 4.14 shows Ag K edge spectra taken when O_2 was absent in the reaction mixture and when the ethanol/O_2 ratio was 1/2. The temperature dependence of the XANES under reaction conditions can be identified from this figure. As discussed in the previous section, both oxidation and thermal damping affect the Ag K edge spectrum in very similar ways. Comparison of the spectra taken at 25 °C before and after increasing the temperature suggests that no change takes place when the ethanol/O_2 ratio was 1/0. However, at an ethanol/O_2 ratio of 1/2, a remarkable mismatch of these spectra due to partial oxidation can be observed. The spectra taken at an ethanol/O_2 ratio of 1/1 are given in figure 2 in the appendix.

The dependence of XANES on the O_2 partial pressure indicates interaction and charge transfer from Ag to O_2. Hence, Ag could be responsible for enhanced O_2 activation in the bimetallic catalysts.

It must be born in mind that the changes in the Ag K edge spectra are small and that most of the Ag remains reduced under reaction conditions. Most probably this is because only Ag atoms on the particle surface are

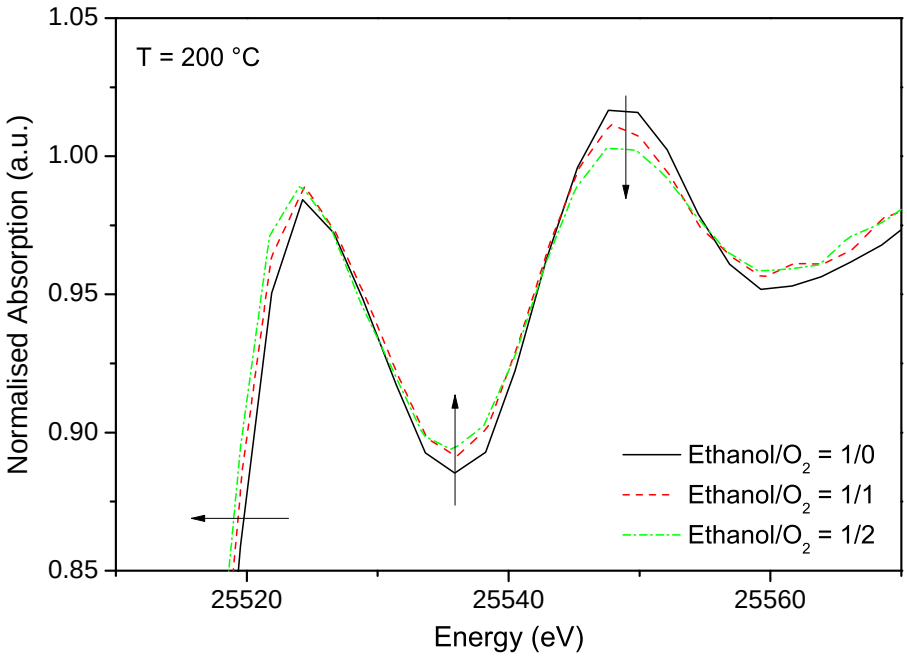

Figure 4.13. Ag K edge XANES recorded under the reaction conditions ethanol/O_2 = 1/1 (top) and during reaction at 200 °C at different ethanol/O_2 ratios (bottom). Arrows indicate changes in the spectrum ascribed to increasing O_2 partial pressures.

accessible for O_2. However, operando XAS measurements only cover a short time period and further oxidation of Ag can not be excluded.

Results of kinetic tests indicate that both the monometallic and bimetallic catalysts are deactivated upon heating up. In the XANES, no clear cause for this effect can be found.

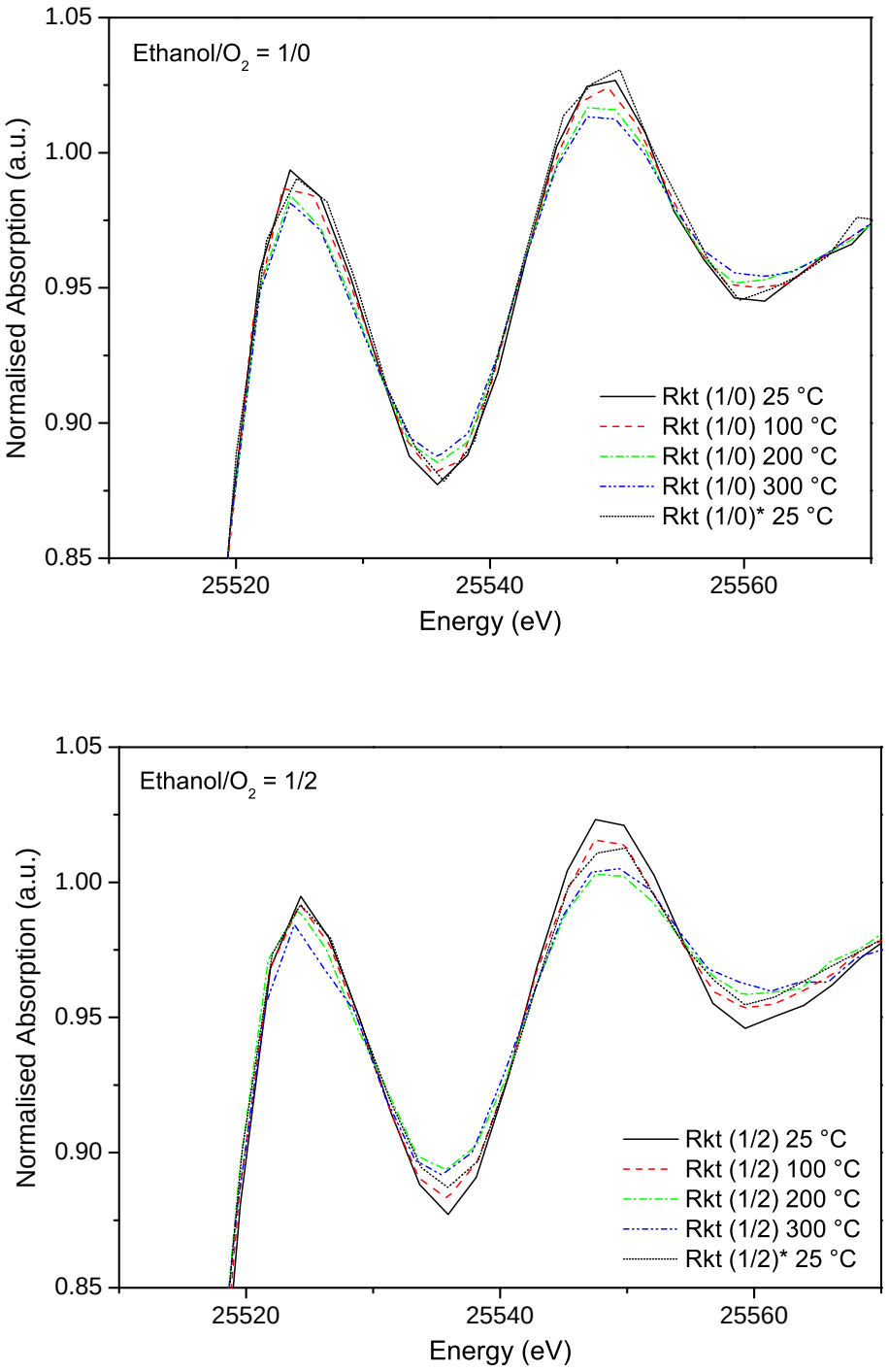

Figure 4.14. Temperature dependence of the Ag K edge XANES under reaction conditions; ethanol/O_2 ratios of 1/0 (top) and 1/2 (bottom). After heating up stepwise to 300 °C the temperature was reduced and spectra were taken at 25 °C (dotted line).

4.3.2 EXAFS

The EXAFS contains information about the local environment of an element and allows the determination of the number and type of its nearest neighbors. In this section results of fitting the Ag K edge EXAFS will be discussed, focusing on the determination of coordination numbers (CN). Single path fits of the Ag-Au and Ag-Ag coordination were performed. In addition, a mixed first shell model including both of these scattering paths and a fixed total coordination number was employed to study the distribution of Ag and Au.

The EXAFS signal of the Ag foil and the TiO_2 Au(4)Ag catalyst after reduction is given in figure 4.15. Compared to bulk Ag, the signal gets increasingly noisy and oscillations fade quickly at higher energies, which is typical of small particles. The reduced intensity in the Fourier transform (FT) can mainly be attributed to reduced coordination numbers, increased structural disorder and the presence of Au.

There are three basic reasons why XAFS measurements in a Au host are generally of lower quality compared to a Ag host [50] : First, Au is sufficiently heavier than Ag that its absorption cross-section is generally higher than that of Ag. This means that the measured absorption signal is dominated by Au. Second, Au is softer than Ag so that thermal damping of the Au backscattering is larger for Au. Thirdly, Au has a deep and fairly broad minimum in its backscattering amplitude $F(k)$ at k $\approx$ 5-7 $Å^{-1}$. The combination of these effects severely limits the k-range of useful data.

Generally, interatomic distances appear about 0.2–0.5 Å shorter than the actual distance in the Fourier transform, which is due to the energy dependence of the phase factors $\phi(k)$ in the argument of the sine in the EXAFS function (see equation 2.8). The distance to the nearest neighbor is 2.8921 Åin bulk Ag and is found at 2.67 Åin the FT of the foil data. The peak in the R space spectrum of the Ag foil (figure 4.15) is not an atom at distance 2.13 Å(Ag foil) and 2.23 Å(Red A* 25 °C), but due to the phase shift. The two peaks at 2.23 and 2.79 Åin the Red A* 25 °C spectrum can be assigned to Au and Ag atoms. This assignment is based on single path fits.

The distance to the first neighbor in bulk Au is 2.8850 Å. The peak at 1.3 Åis neither a Ag nor a Au scattering contribution and could be assigned to a Ag-O coordination of adsorbed species or of the support but it could also be an artefact.

A fit of the spectrum taken after the first reduction (Red B* 25°C) with the mixed first shell model is given in figure 4.16. Ag-Ag and Ag-Au single

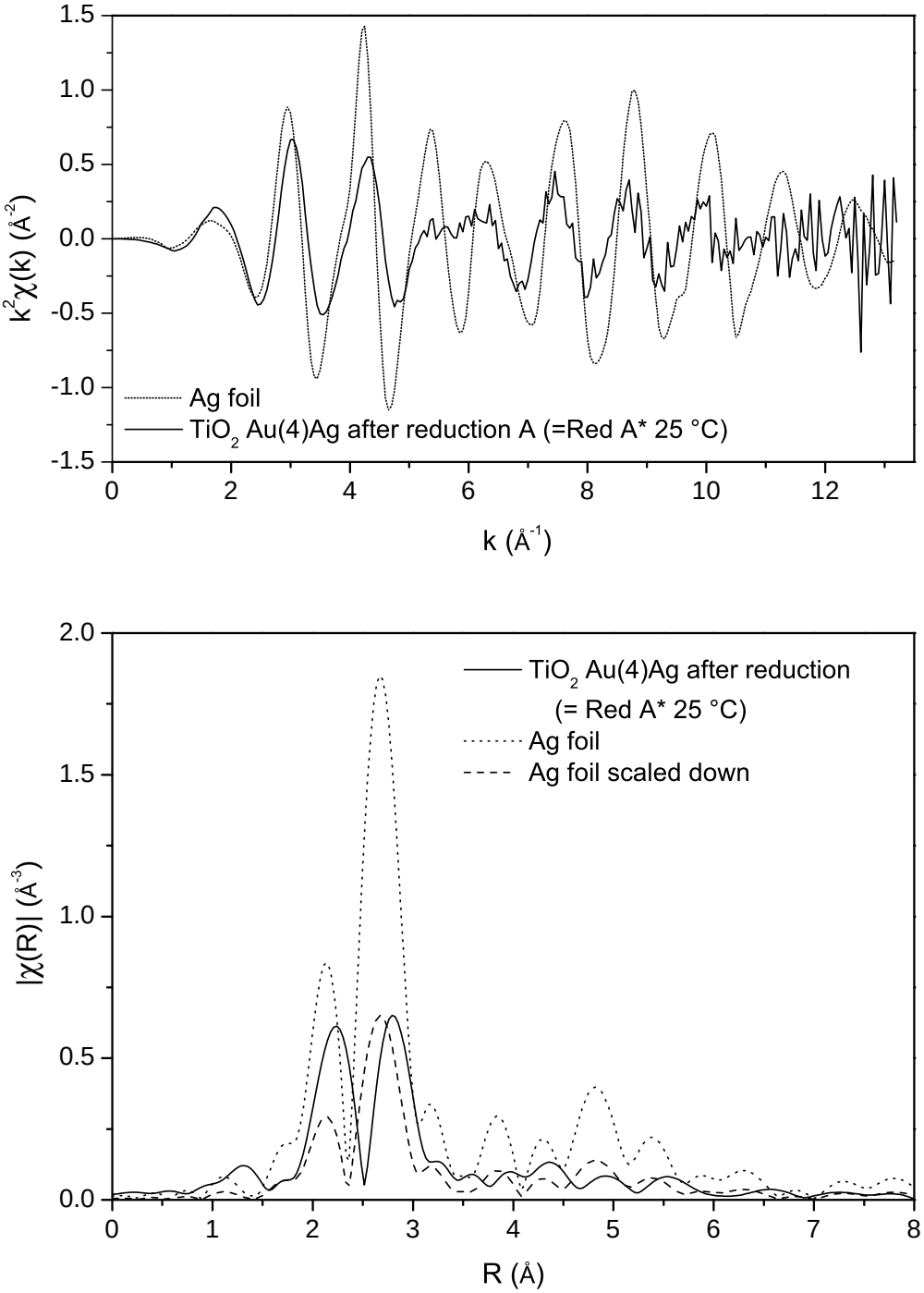

Figure 4.15. Ag K edge EXAFS (top) of the reduced sample (after reduction Red A* 25 °C) and the magnitudes of their FT (bottom); k-weight 2.

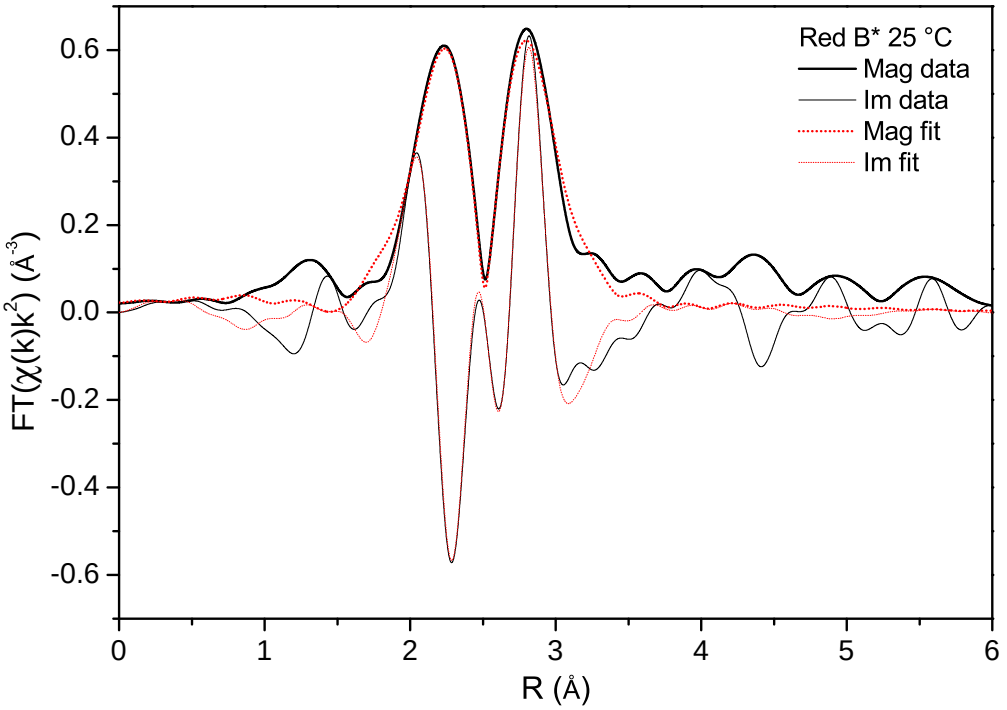

Figure 4.16. Mixed first shell fit of the Ag K edge spectrum taken after the first reduction (Red B*25°C).

path fits of the same dataset are shown in figure 4.17. CN obtained from single path fits are shown in figures 4.18 and 4.19 together with the CNs obtained with the mixed first shell model.

In general, the single path fits yield "bad" fits with elevated values for goodness of fit parameters. Without exception, the R factor exceeds the recommended value of R $<$ 0.05. Moreover, Single path fits of the Ag-Ag path often give physically unreasonable CNs. In contrast, results of the Ag-Au single path fits are physically reasonable in most cases and CNs are in good agreement with the results of the mixed first shell model fits.

For the most part, the mixed first shell model gives very good fits and physically reasonable results. Results of all fit variables of the determination of Ag-Au CNs are summarized in table 1 for the single path fits and in table 2 for the mixed first shell model. The constant S_0^2 is an important source of uncertainty: it strongly influences the value of x. Using the lattice parameter of Ag (4.090 Å instead of 4.080 Å) for FEFF calculations yields similar values for coordination numbers. However, results from the Au model give a better match, i.e. lower values for R and χ^2_{red}. In addition, the dependence

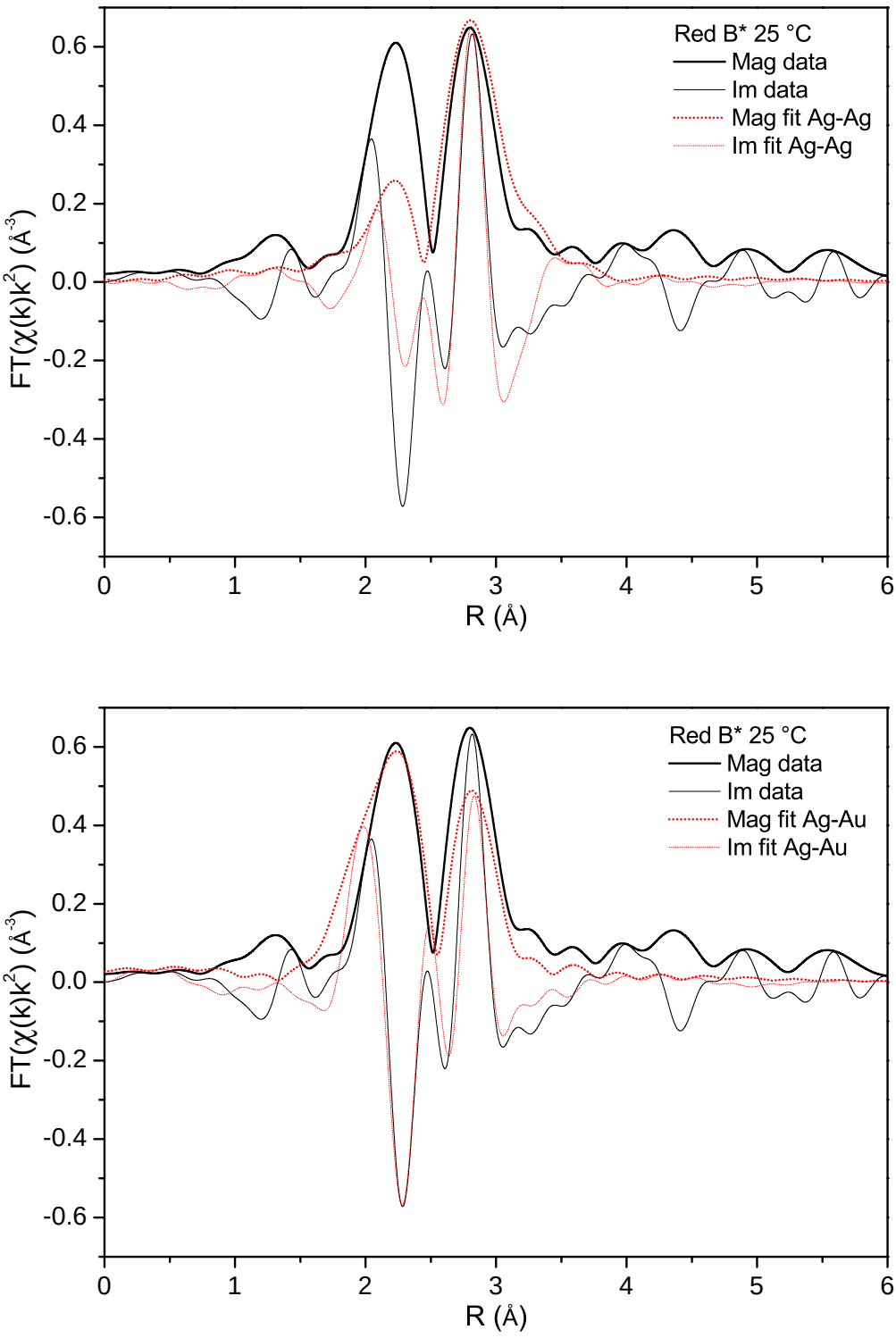

Figure 4.17. Single path Ag-Ag (top) and single path Ag-Au fits (bottom). Spectrum taken after first reduction (Red B* 25 °C).

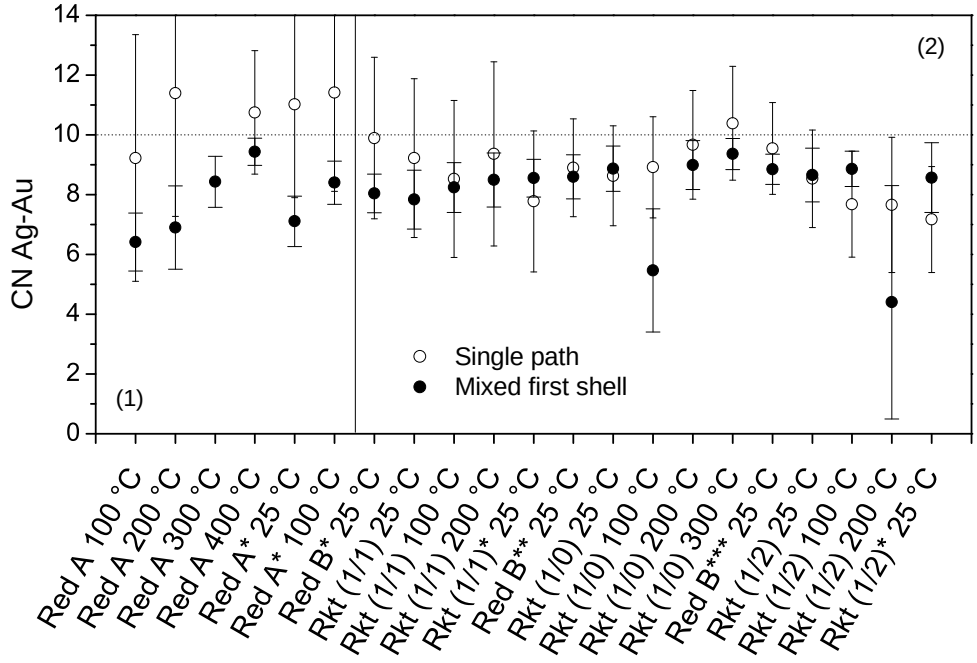

Figure 4.18. Ag-Au CN from single path and mixed first shell model fits. Two pellets (1) and (2) were used in the experiments.

on S_0^2 is less pronounced.

The correlation of the Debye-Waller factor σ_j^2 with the coordination number N_j is ignored in the mixed first shell model. A substantially higher value is observed in highly disordered systems like nanoparticles. The values of ss and ss_1 in table 2 are in agreement with this. The increase of Debye-Waller factors due to thermal disorder is in agreement with theory.

The goodness of fit parameters strongly depend on the fitting range and also on the number of free variables. The more variables are refined, the better the fit. It is apparent from figures 4.18 and 4.19 that results for CN are strongly temperature dependent. For example, the mixed first shell model yields an apparent increase of 1.3 of the Ag-Au CN when heating up from 25 to 100 °C after reduction A.

Interatomic distances of Ag-Au are lower than Ag-Ag. At 25 °C distances are reduced significantly relative to the Au lattice constant by up to 0.03 Å, which corresponds to about 1 %. EXAFS allows the determination of interatomic distances with an accuracy of less than ± 0.01 Å. In some cases, the interatomic distances are not correlated with temperature. Reduced

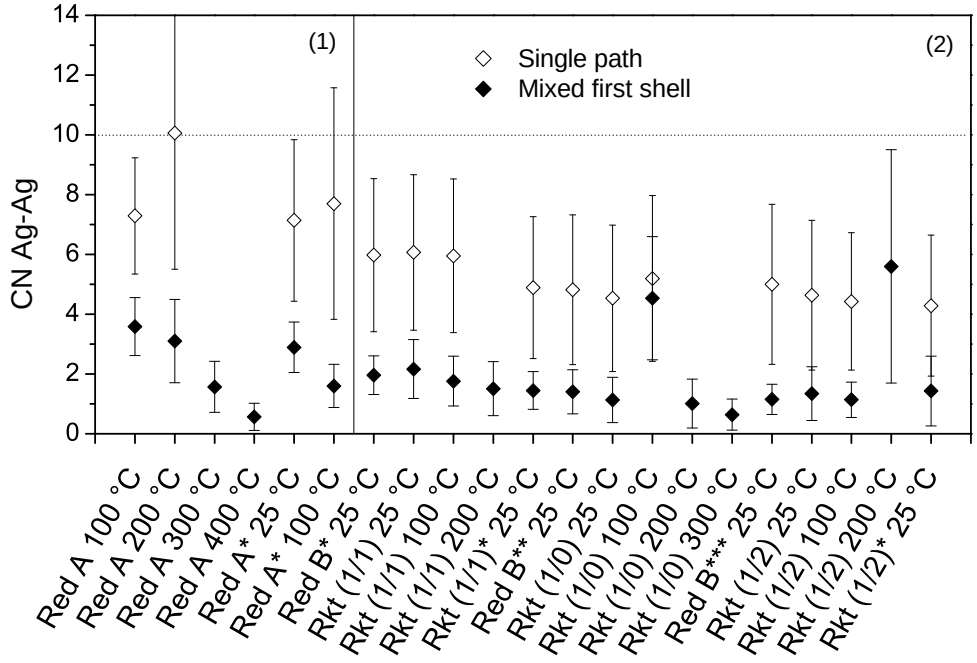

Figure 4.19. Ag-Ag CN from single path and mixed first shell model fits. Two pellets (1) and (2) were used in the experiments.

interatomic distances can be caused by the large number of surface atoms; in general, lower interatomic distances are measured in nanoparticles.

The lattice constant of the alloy system Au-Ag is lower than predicted by Vegard's law [27]. Local deviations of the fcc structure were not detected in a bulk 1:1 Ag-Au alloy [51].

Comparison of results of the fits after reduction (Red B* 25°C) suggests that there is a small increase of Ag-Au CN in the course of the experiment. Thus, alloy formation might not be completed after reduction and a more homogeneous alloy is formed upon further thermal treatment. On the other hand, this could also be related to changes in particle size or shape.

The Ag-Au CN of a perfectly random 4/1 AuAg alloy nanoparticle with an average total CN of 10 is 8.8. Within uncertainties, CN determined with the mixed first shell fits are in good agreement with this value. From CN measured after reduction it may be concluded that reduction B is more favourable to alloy formation than reduction A. Only with the constraint $\sum N_{A-i} = 10$ physically meaningful results for both Ag-Au and Ag-Ag CN are obtained.

Thus, application of the model described in 2.3.4 is limited. Unfortunately, Au-Ag and Au-Au CN could not be studied because of the poor quality of the spectra (glitches). Nevertheless, a value of $J_{Ag} \leq 100$ can be determined. Given the deviation of the Au-Ag system from Vegard's law, Ag-Au interactions are stronger than Au-Au interactions in bulk alloys.

Evaluation of EXAFS cleary indicates alloy formation. However, as XAFS only gives average information on the local structure, only the average extent of alloy formation is obtained. This means that the same result is obtained from samples in which all particles exhibit the same Ag/Au content as well as from samples with unequal Ag/Au ratios. The average CNs do not contain information on the composition of individual particles.

4.4 Infrared Spectroscopy

Infrared spectroscopy is ideally suited for the qualitative characterization of catalytically active materials. It allows to study the chemical nature of catalysts, to probe available adsorption sites, identify adsorbed species and investigate the strength of the chemical bond to a catalyst surface. Carbon monoxide is a widely used probe molecule for the investigation of metal and oxide surfaces. The C=O stretching frequency (2143 cm^{-1} in the gas phase) occurs in a region where most catalysts are transparent. CO is an ideal probe molecule for oxide surfaces because CO adsorption occurs with the participation of surface oxygen, hydroxyl groups and coordinatively unsaturated surface cations.

The aim of FTIR measurements is to identify differences between mono- and bimetallic catalysts in their adsorption behaviour. In this section the adsorption of CO on TiO_2 Au(2)Ag, and TiO_2 Au(2)Ag after reduction at 400 °C in 5 % H_2 (reduction A) will be discussed.

4.4.1 Adsorption Sites

Peaks of CO adsorbed on oxide surfaces are observed in two regions, namely within the carbonate-carboxylate region at 300-1700 cm^{-1} and between 2000-2200 cm^{-1}. Peaks in the 2000-2200 cm^{-1} region are characteristic of reversible CO adsorption arising from interactions with surface cations.

Absorption peaks of CO species adsorbed on metals appear between 1650 and 2200 cm^{-1}. Wavenumber ranges can be assigned to specific adsorption geometries, i.e. degrees of coordination on the metal atoms like "on top" and in bridging positions between metal atoms.

CO Adsorption on TiO_2

Hadjiivanov and Vaysillov have published an extensive review about CO adsorption on oxide-supported materials commonly applied as heterogeneous catalysts [52]. According to this review, bands at 2215-2163 cm^{-1} should be attributed to $Ti^{4+}-CO$ surface complexes. The attribution to $Ti^{3+}-CO$ is contested because also on oxidised samples where $Ti^{3+}-CO$ is absent carbonyl bands occur in this region.Bands at 2110-2115 cm^{-1} are considered to be characteristic of $Ti^{3+}-CO$ species. Ti^{4+} ions are coordinated only by electrostatic interaction and a σ bond because π back-donation does not take place in a d^0 electron configuration.

$Ti^{4+}-CO$-bands have also been reported at 2151-2156 cm^{-1} . The interaction of CO as a weak base with surface hydroxyl groups by formation of an $OH-CO$ species gives rise to bands at 2150-2178 cm^{-1} that are only present at low temperatures. The more acidic the OH groups, the higher the wavenumber of the CO band. On TiO_2 these bands have been observed at 2155 and 2158 cm^{-1} on anatase and at 2150 cm^{-1} on rutile.

On anatase, a stronger bonding site and a weaker bound Ti^{4+} site give rise to CO stretching frequencies at 2208 cm^{-1} and 2186-2195 cm^{-1} that are observed at room temperature [52]. Upon CO adsorption at low temperatures on reduced rutile, a band at 2182 cm^{-1} occurs. On oxidized rutile, this band is observed at 2178-2192 cm^{-1} [52].

CO Adsorption on Au and Ag

On reduced samples, no $Ag-CO$ carbonyls are observed. The low strength of the $Ag(0)-CO$ bond has also been evidenced by theoretical calculations. On oxidised Ag/TiO_2 adsorption of CO gives a band at 2161 cm^{-1} [53].

It is generally accepted that CO adsorbed on Au(0) particles supported on TiO_2 give a sharp band at 2105-2130 cm^{-1}. On Au/TiO_2 prepared by DP and an average particle size of 3.5 ± 0.8 nm two types of adsorption sites can be distinguished: bands at 2106-2118 cm^{-1} are related to Au atoms not at the periphery of the particle, whereas bands at 2090-2110 cm^{-1} are assigned to Au atoms at the periphery of the particles, indicating the influence of the support.

4.4.2 Band Assignation

Figure 4.20 contains spectra taken at -115 °C after admission of 5 mbar CO. The band at 2210 cm^{-1} can be assigned to strong (α) Ti^{4+} cation sites (uncoordinated and defective sites); the main peak at 2176-2178 cm^{-1} is assigned to weak (β) sites on the anatase (0 1 0) face [53].

The band at 2152-2155 cm^{-1} is due to interactions of surface hydroxyl groups with CO. The absence of this band in the TiO_2 Au(2) sample may be due to longer evacuation before CO adsorption.
The CO-Au(0) band occurs at 2098 cm^{-1} in the TiO_2 Au(2) sample and is slightly shifted to 2100 cm^{-1} in the TiO_2 Au(2)Ag catalyst. It can be clearly assigned to linearly adsorbed CO on Au [52, 53, 54].
There are no CO-metal bands below 2000 cm^{-1}. Apparently, at -115 °C CO only adsorbs linearly on Au on both the mono- and the bimetallic catalysts.

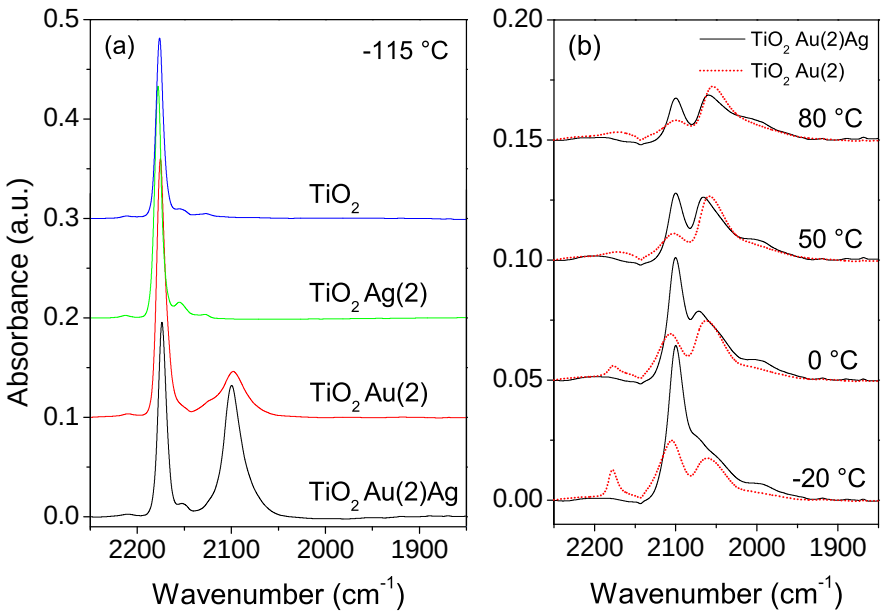

Figure 4.20. Details of IR spectra of reduced TiO_2 Au(2) and Au(2)Ag catalysts and reference materials after admission of 5 mbar CO at -115 °C and during warming up.

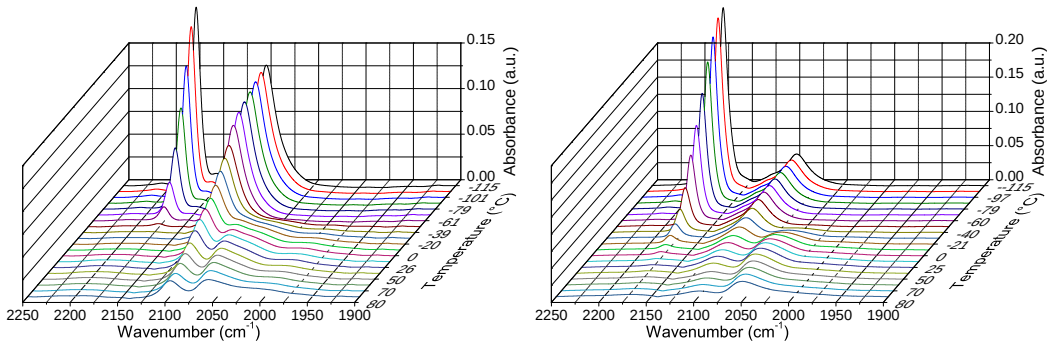

(a) TiO_2 Au(2)Ag (b) TiO_2 Au(2)

Figure 4.21. Evolution of surface carbonyl bands on freshly reduced TiO_2 catalysts while warming up after introduction of 5 mbar CO at -115 °C.

The evolution of the carbonyl bands while warming up in CO are given in figure 4.20 b) and figure 4.21. The bands that occur at around 1990-2073 cm^{-1} at higher temperatures have also been observed by Boccuzzi et al. [55] who studied the pressure dependence of CO adsorption on reduced Au/TiO_2 catalysts. They propose that the formation of a band at 2055 cm^{-1} can be

ascribed to adsorption sites on very small Au clusters. They suggest that electron transfer from the reduced support to very small Au clusters could allow back donation to CO and thus shifts the CO vibration frequency and stabilises bridge-bonded CO at low coverages. This proposal is based on reports of CO absorption bands at 2050-1950 cm^{-1} on gold electrodes during the electrooxidation of CO at negative potentials. CO on these small clusters appears to be more strongly bonded than CO on larger particles. They assigned the 1990 cm^{-1} band to bridge bonded CO and the band at 2055 cm^{-1} to linearly adsorbed CO. At decreasing CO coverage, the band ascribed to bridge bonded CO grows and the one ascribed to linear bonded CO decreases.

A difference in adsorption behaviour between Au(2) and Au(2)Ag catalyst can be observed in the relative intensities of the peaks at 2050 and 2100 cm^{-1}. A rather broad and weak band at 1997-2000 cm^{-1} is more pronounced on the TiO_2 Au(2)Ag catalyst. These are indications that the addition of Ag to Au alters its adsorption properties. Similarly to small Au clusters, a further explanation could be the transfer of electron density from Ag to Au, which has a higher electron affinity, as a consequence of alloy formation.

Interpretation of CO adsorption can be complicated because the CO stretching frequency is influenced by a number of parameters. Further measurements of the pressure- and temperature dependence of CO adsorption of reduced and oxidised samples will contribute to elucidate the adsorption properties of AuAg alloy nanoparticles.

4.5 X-Ray Photoelectron Spectroscopy

XPS provides information of the elemental identity, chemical state, and quantity of an element based on the photoelectric effect. As the mean free path of electrons in a material is limited, the XPS signal stems from the surface of the sample,typically the first atomic layers.

In this section results of XPS measurements of TiO_2 supported AuAg catalysts will be discussed. Samples were taken from the fixed bed reactor for kinetic measurements before and after exposure to reaction conditions.

4.5.1 Experimental Procedure

The samples were used directly after reduction or reaction and pressed onto a piece of Al-foil to minimize charging effects in the XPS spectra. After mounting the Al-foil to a sample holder plate, the samples were introduced to a Load Lock, which was evacuated to a pressure below 10^{-7} mbar. Then the samples were introduced to the UHV main chamber and positioned in front of the X-ray source and analyzer. As no further oxidative or reductive treatments could be performed, all samples were contaminated with carbon and always peaks related to the Al-foil substrate could be identified in the spectrum. Remaining charging effects were corrected by setting the Ti^{4+} 2p 3/2 peak to a binding energy of 459.2 eV[1]. The observed charging was low for the freshly reduced samples but shifts of about 2.5 eV were detected for the samples measured after reaction due to dilution with silica. Measurements were performed with Mg K_α X-ray source (1254 eV). The software XPS-Peak was used for peak fitting.

4.5.2 Surface Composition

The complete XPS spectrum of the reduced TiO_2 Au(4)Ag catalyst is displayed in figure 3 in appendix A; high resolution scans are given in figures 4.22 and 4.23. Element ratios were determined from peak areas and atomic sensitivity factors (table 5). Peak positions and areas of the bimetallic samples are given in tables 3 and 4 in appendix A. Element ratios are listed in table 4.5. Unfortunately, Ag was not detected in the TiO_2 Au(4)Ag sample after reaction.

The inelastic mean free path of photoelectrons at 1200 eV is 1.63 nm for Ag and 1.48 nm for Au [56]. Approximately 63 % of the signal originates from this depth at a normal takeoff angle. At different angles, the sampling depth

[1]Moulder JF, Stickle WF, Sobol PE, Bomben KD (1995) Handbook of X-ray Photoelectron Spectroscopy. Physical Electronics, Inc.

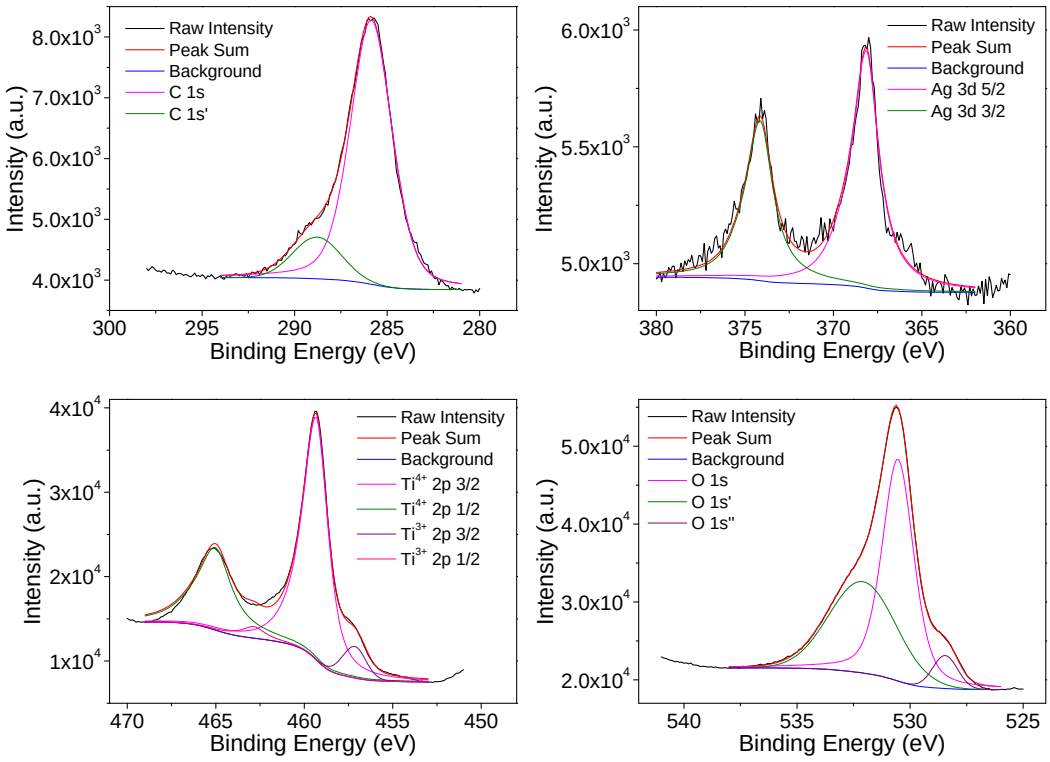

Figure 4.22. XPS spectrum of the reduced TiO_2 Au(4)Ag catalyst.

	TiO_2 Au(4)Ag reduction	TiO_2 Au(4)Ag reaction	TiO_2 Au(4) reaction
Au/Ti	$6.34 \cdot 10^{-2}$	$5.46 \cdot 10^{-2}$	$9.56 \cdot 10^{-2}$
C/Ti	1.53	2.93	4.59
O/Ti	2.15	6.47	6.9
Ag/Ti	$2.15 \cdot 10^{-2}$		
Au/Ag	2.95		

Table 4.5. Element ratios determined by XPS.

is lower. It is difficult to estimate the sampling depth of powder samples, but it is very likely that a smaller fraction of the signal stems from the surface given average particle sizes of about 2 nm.

The Au/Ag ratio of the reduced TiO_2 Au(4)Ag catalyst is considerably lower than the expected average Au/Ag ratio[2] of 4/1. Hence, the concentra-

[2]The Au/Ag ratio could not be determined by means of atom absorption spectroscopy

tion of Ag on on the catalyst surface is elevated significantly.

The segregation of Ag to the surface of AuAg alloys has been observed on a number of well defined surface planes and was also found by Bozzolo et al. [27] using computational methods. Kim et al. [28] employed surface enhanced Raman scattering (SERS) to study the surface of AuAg alloy nanoparticles and found strong evidence of elevated Ag concentrations on the particle surface.

4.5.3 Oxidation States

Shifts caused by electron transfer due to AuAg alloy formation are not observed in the XPS spectra. Ti^{3+} and Ti^{4+} species can be identified in the spectra, strongly indicating the partly reduced state of the support material.

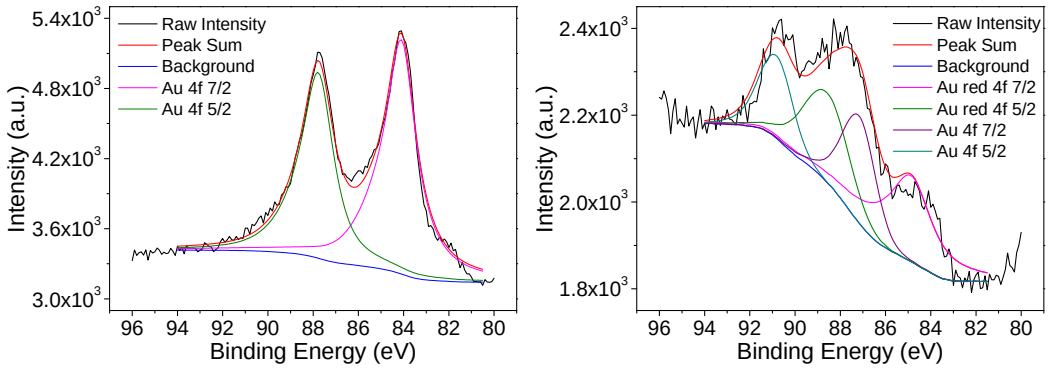

Figure 4.23. XPS spectrum of the TiO_2 Au(4)Ag catalyst after reduction (left) and after reaction (right).

In figure 4.23 a comparison of the Au 4f XPS spectrum of the freshly reduced TiO_2 Au(4)Ag catalyst and the spectrum taken after reaction at 300 °C is given: In the freshly reduced TiO_2 Au(4)Ag sample only metallic Au was detected. Differently, the spectrum of the used sample exhibits Au 4f peaks that are shifted towards higher binding energies. This is surprising as no indications of oxidised Au were found in XAS measurements. It should be noted that this spectrum is noisy and that peak intensities are lower compared to the freshly reduced TiO_2 Au(4)Ag sample, which can be explained by the large amount of carbon. For the same reason, Ag could not be detected in the used catalyst.

(AAS) due to precipitation of nitrates upon aqua regia digestion. It is assumed that all Au was deposited on the support in the synthesis.

Chapter 5

Summary and Conclusions

The selective partial oxidation of bioethanol could be used as a pathway to produce bulk chemicals such as acetaldehyde, acetic acid and butadiene from renewable feedstocks. In the development of highly selective heterogeneous oxidation catalysts, nanoparticulate Au is a promising candidate.

The main goal of this thesis was the synthesis and characterization of Au and AuAg catalysts supported on TiO_2 and ZrO_2 for the selective gas-phase partial oxidation of ethanol. The properties of mono-and bimetallic catalysts prepared by different preparation methods were investigated.

The catalysts were prepared by deposition-precipitation of $HAuCl_4$ with urea, Ag was deposited by incipient wetness impregnation with $AgNO_3$. Two strategies were used to prepare catalysts with a Au loading of 2 and 4 % and a Au/Ag ratio of 4/1: Firstly, both metals were deposited in an oxidised state by subsequent deposition of Au and impregnation with $AgNO_3$. Secondly, $AgNO_3$ was added first and reduced in a H_2 flow before the deposition-precipitation of Au.

Upon reduction in a flow of H_2 at 300 °C, particles that are well dispersed were formed on TiO_2. On ZrO_2, particle size and dispersion was less than ideal. Particle size depends on reduction conditions. At a lower H_2 flow rate larger particles were obtained.

The reactivity of the catalysts was investigated at 100, 200 and 300 °C at an ethanol/O_2 ratio of 1/1. Under these conditions, acetaldehyde is formed at high selectivities. The main side product is ethyl acetate. The bimetallic catalysts supported on TiO_2 exhibited a higher ethanol conversion than the monometallic ones, which can be explained by the higher total metal loading of the bimetallic catalysts. The difference in activity was similar to the activity of a comparable Ag catalyst. In terms of activity, adding Ag first in

the preparation was advantageous. The selectivity to acetaldehyde of TiO_2 based catalysts was above 90 % for all samples. In terms of selectivity, adding Au first was advantageous: At 200 °C, selectivities to acetaldehyde of up to 98 % were obtained.

The selectivity of bimetallic catalysts with Ag deposited first was higher on TiO_2 than on ZrO_2. In the case of ZrO_2 supported catalysts, the highest conversion, selectivity, but also deactivation was observed in the monometallic Ag catalyst. The presence of Au leads to higher stability but lower selectivity. In the TiO_2 bimetallic catalyst no significant change in particle size was observed after exposure to reaction conditions at 200 °C . Deactivation upon performing the reaction at 300 °C might be rather related to changes in particle morphology than particle size. Unsuccessful reactivation by reduction in H_2 suggests an irreversible deactivation mechanism.

Dehydrogenation of ethanol on mono- and bimetallic TiO_2 supported Au and AuAg catalysts yields lower selectivities. Moreover higher temperatures were necessary due to the endothermic character of the reaction.

In order to investigate the structure of the materials during reduction and under reaction conditions, operando XAS measurement were performed at the Ag K and Au L_{III} edges. Linear combination fits of XANES recorded during temperature programmed reduction experiments showed that the reduction of both metals is completed at similar temperatures. In a temperature programmed oxidation experiment, Au remained metallic whereas Ag was oxidised. Under reaction conditions, the interaction of O_2 with Ag is clearly reflected in the Ag K edge XANES and there are indications of the presence of oxidised Ag. This indicates the role of Ag in the activation of O_2.

Evidence of alloy formation was found in the EXAFS of the Ag K edge: A model containing two scattering paths and a set total coordination number was employed to determine Ag-Au and Ag-Ag coordination numbers of the first coordination shell.

Although surface atoms make a considerable contribution to the spectrum in the case of very small particles, XAS reveals bulk structure. Therefore more surface sensitive characterization methods were employed to characterize surface composition and available adsorption sites.

In situ FTIR measurements of CO adsorption on freshly reduced TiO_2 catalysts showed the formation of a new band at 2055 cm^{-1} upon heating up from -115 °C. A possible explanation is the formation of negatively charged metal clusters on the reducible support. Due to the weak interaction of CO and Ag no Ag surface carbonyls were observed. Differences between mono-

and bimetallic samples included small and rather broad bands in the region typical of bridge-bonded CO.

XPS measurements performed after reduction showed a substantially reduced Au/Ag ratio of 2.95 compared to the expected average composition, which could be an indication of the segregation of Ag to the surface of alloy particles. The shift of the Au 4f peaks might be an indication of oxidised Au species. However, in the results of X-ray absorption spectroscopic measurements indications of oxidised Au were absent.

Apart from EDX TEM, the spectroscopic methods employed in this thesis only provide average information of a large number of nano-particles. Further measurements using TEM and a more powerful EDX detector would be highly desirable to investigate the composition of individual particles after reduction and reaction.

Further studies targeting a better understanding of the mechanism of ethanol oxidation on bimetallic catalysts can be extended to the investigation of surface species under reaction conditions using in situ FTIR measurements. It would be useful to perform high pressure XPS measurements and further operando XAS studies to detect oxidised Au and Ag species and further study the structure of bimetallic nano-particles.

Especially interesting would be the performance of time resolved FTIR and XAS measurements in the framework of concentration modulation experiments employing phase sensitive detection.

Appendix A Spectra and Tables

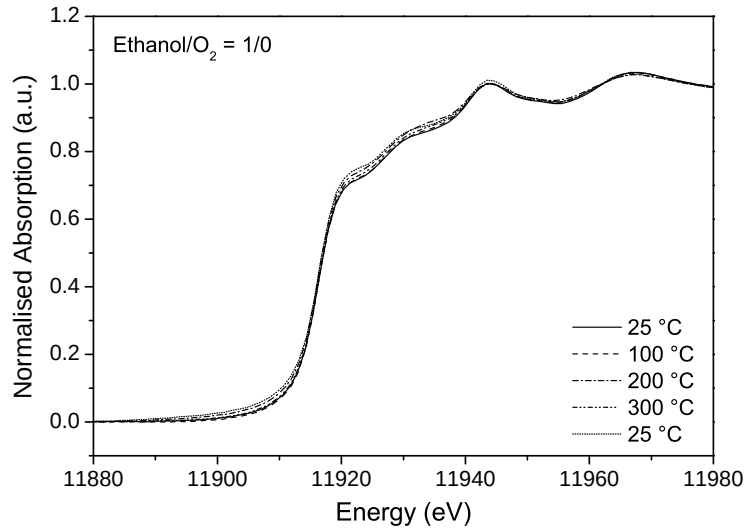

Figure 1. Au L_{III} edge XANES of the TiO_2 Au(4)Ag catalyst under reaction conditions; ethanol/O_2 = 1/0.

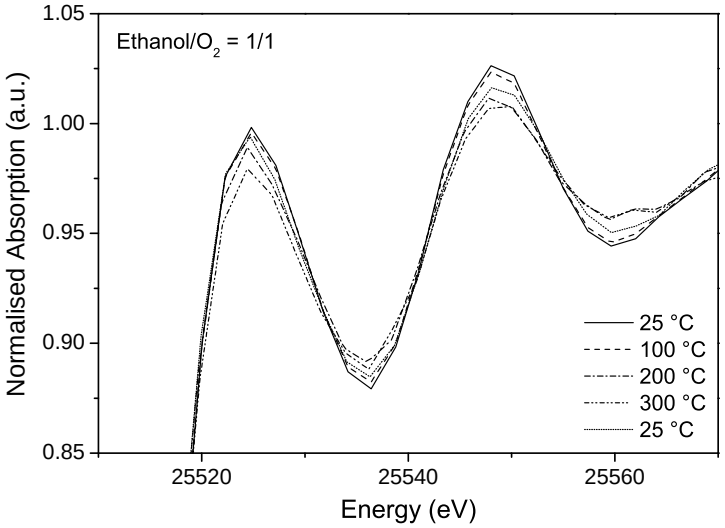

Figure 2. Ag K edge XANES of the TiO_2 Au(4)Ag catalyst under reaction conditions; ethanol/O_2 = 1/1.

Fit	R-factor	χ^2_{red}	enot (eV)	delr (Å)	ss (Å^2)	CN(Au)	CN (Au) ±
Red A 100 °C	0.2994	50.0	-1.8	-0.098	0.016	9.2	4.1
Red A 200 °C	0.2066	37.3	-0.5	-0.072	0.023	11.4	4.1
Red A 300 °C	0.1097	8.8	2.0	0.006	0.037	16.2	5.9
Red A 400 °C	0.0555	4.4	1.1	-0.043	0.028	10.8	2.1
Red A* 25 °C	0.1456	37.7	-1.0	-0.077	0.015	11.0	3.1
Red A* 100 °C	0.1533	29.0	-1.0	-0.075	0.018	11.4	3.3
Red B* 25 °C	0.134	15.1	-0.6	-0.074	0.014	9.9	2.7
Rkt (1/1) 25 °C	0.1503	37.9	-0.4	-0.062	0.015	9.2	2.7
Rkt (1/1) 100 °C	0.1729	16.0	0.2	-0.052	0.017	8.5	2.6
Rkt (1/1) 200 °C	0.1729	8.2	1.3	-0.026	0.024	9.4	3.1
Rkt (1/1)* 25 °C	0.1656	26.5	-0.0	-0.066	0.015	7.8	2.4
Red B* 25 °C	0.0644	14.2	0.2	-0.066	0.013	8.9	1.6
Rkt (1/0) 25 °C	0.0718	21.3	0.2	-0.063	0.013	8.6	1.7
Rkt (1/0) 100 °C	0.073	30.1	0.5	-0.056	0.016	8.9	1.7
Rkt (1/0) 200 °C	0.0697	5.8	0.6	-0.048	0.021	9.7	1.8
Rkt (1/0) 300 °C	0.059	10.4	0.9	-0.039	0.024	10.4	1.9
Red B* 25 °C	0.0517	11.1	0.5	-0.060	0.014	9.5	1.5
Rkt (1/2) 25 °C	0.0704	22.9	0.2	-0.060	0.013	8.5	1.6
Rkt (1/2) 100 °C	0.1041	18.7	0.5	-0.056	0.016	7.7	1.8
Rkt (1/2) 200 °C	0.1516	6.9	1.3	-0.036	0.022	7.7	2.3
Rkt (1/2)* 25 °C	0.1165	6.9	1.2	-0.040	0.014	7.2	1.8

Table 1. Results of EXAFS fits, Ag-Au path only. The number of independent points is 10, the number of free parameters 4 for each fit. Starting values for ss and ss_1 were 0.003 and 10 for the Au CN parameter; they were 0 for delr and enot .*) at the end of the temperature programme (see 3.5).

Fit	R-factor	χ^2_{red}	enot (eV)	delr (Å)	ss (Å^2)	enot_1 (eV)	delr_1 (Å)	ss_1 (Å^2)	x	x +/-
Red A 100 °C	0.0169	5.29	2.9	-0.015	0.019	1.3	-0.025	0.012	0.4	0.1
Red A 200 °C	0.0219	7.44	2.2	-0.042	0.020	0.6	-0.038	0.015	0.3	0.1
Red A 300 °C	0.0195	2.92	2.3	-0.025	0.025	-0.7	-0.067	0.013	0.2	0.1
Red A 400 °C	0.0172	2.54	1.9	-0.032	0.027	1.4	-0.019	0.009	0.1	0.0
Red A *25 °C	0.0121	5.86	1.3	-0.036	0.014	2.3	-0.016	0.011	0.3	0.1
Red A*100 °C	0.0231	8.20	1.6	-0.027	0.016	-0.0	-0.050	0.007	0.2	0.1
Red B* 25 °C	0.0139	2.94	1.8	-0.025	0.014	2.3	-0.015	0.007	0.2	0.1
Rkt (1/1) 25 °C	0.0257	12.1	2.4	-0.015	0.016	1.1	-0.008	0.010	0.2	0.1
Rkt (1/1) 100 °C	0.0278	4.83	2.9	0.003	0.021	2.4	0.009	0.010	0.2	0.1
Rkt (1/1) 200 °C	0.0368	3.27	3.7	0.006	0.022	-3.6	-0.053	0.012	0.2	0.1
Rkt (1/1)* 25 °C	0.0252	7.56	3.5	-0.006	0.017	-3.3	-0.045	0.007	0.1	0.1
Red B* 25 °C	0.0156	6.44	1.9	-0.039	0.015	1.9	0.002	0.009	0.1	0.1
Rkt (1/0) 25 °C	0.025	13.9	1.5	-0.037	0.017	3.2	0.022	0.007	0.1	0.1
Rkt (1/0) 100 °C	0.0215	16.6	1.4	-0.057	0.012	3.1	0.030	0.032	0.5	0.2
Rkt (1/0) 200 °C	0.0235	3.64	1.9	-0.028	0.022	0.5	-0.007	0.011	0.1	0.1
Rkt (1/0) 300 °C	0.0182	6.05	2.0	-0.021	0.024	-0.2	-0.025	0.009	0.1	0.1
Red B* 25 °C	0.0092	3.71	1.7	-0.038	0.016	3.6	0.019	0.007	0.1	0.1
Rkt (1/2) 25 °C	0.0247	15.1	2.0	-0.032	0.016	0.6	-0.000	0.009	0.1	0.1
Rkt (1/2) 100 °C	0.0218	7.33	2.8	-0.013	0.021	0.2	0.002	0.008	0.1	0.1
Rkt (1/2) 200 °C	0.0964	8.18	2.0	-0.056	0.017	4.6	0.110	0.046	0.6	0.4
Rkt (1/2)* 25 °C	0.0554	6.12	3.7	-0.001	0.018	-2.1	-0.008	0.010	0.1	0.1

Table 2. Results of EXAFS fits (amp = 0.9563310; k [2;11.29],R[1.4;3.2]). The number of independent points is 10 and the number of free parameters 7 for each fit; starting values for ss and ss_1 were 0.003 and 0.2 for x; they were 0 for delr, delr_1, enot and enot_1. *) at the end of the temperature programme.

Peak	Position (eV)	Position shifted (eV)	Distance (eV)	Area (a.u.)	Area, ASF corrected (a.u.)	Area Ratio (eV)	FWHM (eV)
Au 4f 7/2	84.11	83.98		5.812E+03	3.884E+02		1.60
Au 4f 5/2	87.78	87.65	3.67	4.359E+03	2.913E+02	0.75	1.61
C 1s	285.86	285.72		1.416E+04	1.416E+04		2.65
C 1s'	288.79	288.65	2.93	2.236E+03	2.236E+03		3.06
Ag 3d 5/2	368.15	368.09		3.062E+03	1.381E+02		1.71
Ag 3d 3/2	374.15	374.09	6	2.042E+03	9.206E+01	0.667	1.75
Ti^{4+} 2p 3/2	459.34	459.20		7.300E+04	6.530E+03		1.58
Ti^{4+} 2p 1/2	465.04	464.90	5.7	3.650E+04	3.265E+03	0.50	2.20
Ti^{3+} 2p 3/2	457.14	457.01	-2.194	6.898E+03	6.171E+02		1.48
Ti^{3+} 2p 1/2	462.84	462.71	5.701	3.449E+03	3.085E+02	0.50	1.48

Table 3. Results of XPS measurements of sample:TiO_2 Au(4)Ag reduction. Peak positions are shifted by 0.13 eV.

Peak	Position (eV)	Position shifted (eV)	Distance (eV)	Area (a.u.)	Area, ASF corrected (a.u.)	Area Ratio (eV)	FWHM (eV)
Au red 4f 7/2	84.88	82.35		8.031E+02	5.367E+01		2.24
Au red 4f 5/2	88.58	86.05	3.70	6.023E+02	4.025E+01	0.75	2.24
Au 4f 7/2	87.15	84.62	2.28	5.423E+02	3.624E+01		1.64
Au 4f 5/2	90.82	88.29	3.67	4.067E+02	2.718E+01		1.64
C 1s	286.81	284.28		6.566E+03	6.566E+03		3.40
C 1s'	289.80	287.27	2.99	1.873E+03	1.873E+03		4.25
O 1s	533.05	530.52		6.019E+04	1.282E+04		2.88
O 1s'	536.49	533.96	3.44	2.097E+04	4.467E+03		2.77
O 1s"	530.54	528.01		6.340E+03	1.351E+03		1.43
Ti^{3+} 2p 3/2	459.47	456.94		1.031E+04	9.224E+02		1.71
Ti^{3+} 2p 1/2	465.17	462.64	5.70	5.156E+03	4.612E+02	0.50	2.84
Ti^{4+} 2p 3/2	461.73	459.20	461.73	1.116E+04	9.979E+02		2.07
Ti^{4+} 2p 1/2	467.43	464.90	5.70	5.578E+03	4.990E+02	0.50	2.38
Ti x	457.28	454.75		8.145E+02			1.36

Table 4. Results of XPS measurements of the sample TiO_2 Au(2)Ag reaction. Peak positions are shifted by 2.53 eV.

Peak	ASF-Faktor
Au 4f	14.96
Ag 3d	22.18
Ti 2p	11.18
C 1s	1.00
O 1s	4.69

Table 5. Atomic sensitivity factors used for XPS quantitative analysis.

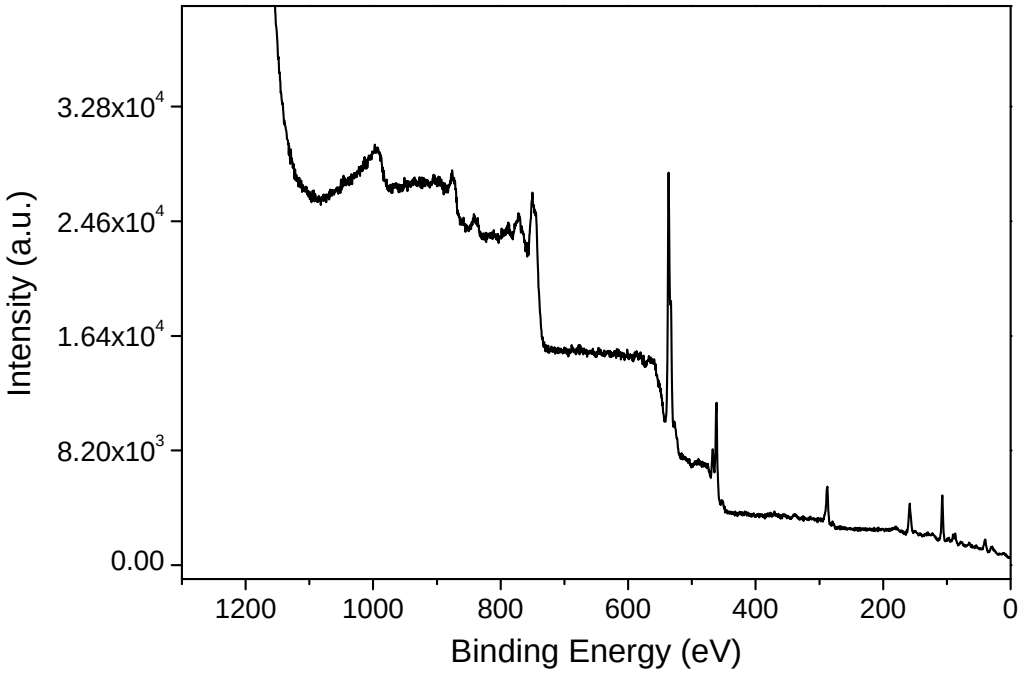

Figure 3. XPS spectrum of the TiO_2 Au(4)Ag catalyst after reaction.

Appendix B Abbreviations

CN	Coordination Number
DFT	Density Functional Theory
DP	Deposition-Precipitation
EDX	Energy Dispersive X-ray Spectroscopy
EXAFS	Extended X-ray Absorption Fine Structure
FID	Flame Ionization Detector
FT	Fourier Transform
HAADF	High Angle Annular Dark Field
HRTEM	High Resolution TEM
IWI	Incipient Wetness Impregnation
STEM	Scanning TEM
TCD	Thermal Conductivity Detector
TEM	Transmission Electron Microscopy
TPO	Temperature Programmed Oxidation
TPR	Temperature Programmed Reduction
XAFS	X-ray Absorption Fine Structure
XANES	X-ray Absorption Near Edge Structure
XAS	X-ray Absorption Spectroscopy
XPS	X-ray Photoelectron Spectroscopy

Bibliography

[1] G. J. Hutchings, "Vapor phase hydrochlorination of acetylene: correlation of catalytic activity of supported metal chloride catalysts.," *Journal of Catalysis*, vol. 96, no. 1, pp. 292–5, 1985.

[2] M. Haruta, T. Kobayashi, H. Sano, and N. Yamada, "Novel gold catalysts for the oxidation of carbon monoxide at a temperature far below 0??C.," *Chemistry Letters*, no. 2, pp. 405–8, 1987.

[3] B.-Z. Zhan and A. Thompson, "Recent developments in the aerobic oxidation of alcohols.," *Tetrahedron*, vol. 60, no. 13, pp. 2917–2935, 2004.

[4] G. C. BOND and D. T. THOMPSON, "Catalysis by Gold," *Catalysis Reviews*, vol. 41, pp. 319–388, Jan. 1999.

[5] G. J. Hutchings and M. Haruta, "A golden age of catalysis: a perspective.," *Applied Catalysis, A: General*, vol. 291, no. 1-2, pp. 2–5, 2005.

[6] J. Edwards, P. Landon, A. F. Carley, A. Herzing, M. Watanabe, C. J. Kiely, and G. J. Hutchings, "Nanocrystalline gold and gold-palladium as effective catalysts for selective oxidation.," *Materials Research Society Symposium Proceedings*, vol. 900E, no. Nanoparticles and Nanostructures in Sensors and Catalysis, pp. No pp. given, Paper : 0900–O01–07–, 2006.

[7] Q. Chen and L. Luo, "Preparation methods of Au-Pd/CeO2 catalysts and properties of partial oxidation of methanol.," *Zhongguo Xitu Xuebao*, vol. 26, no. 1, pp. 12–17, 2008.

[8] A. Corma and H. Garcia, "Supported gold nanoparticles as catalysts for organic reactions," *Chemical Society reviews*, vol. 37, no. 9, pp. 2096–126, 2008.

[9] A. S. K. Hashmi and G. J. Hutchings, "Gold Catalysis," *Angewandte Chemie International Edition*, vol. 45, no. 47, pp. 7896–7936, 2006.

[10] A. K. Hashmi and M. Rudolph, "Gold catalysis in total synthesis," *Chemical Society reviews*, vol. 37, no. 9, pp. 1766–75, 2008.

[11] G. J. Hutchings, S. Carrettin, P. Landon, J. K. Edwards, D. Enache, D. W. Knight, Y.-J. Xu, and A. F. Carley, "New approaches to designing selective oxidation catalysts: Au/C a versatile catalyst.," *Topics in Catalysis*, vol. 38, no. 4, pp. 223–230, 2006.

[12] G. J. Hutchings, M. Brust, and H. Schmidbaur, "Gold–an introductory perspective," *Chemical Society reviews*, vol. 37, no. 9, pp. 1759–65, 2008.

[13] G. J. Hutchings, "Green catalysis with alternative feedstocks.," *Preprints of Symposia - American Chemical Society, Division of Fuel Chemistry*, vol. 53, no. 1, pp. 188–190, 2008.

[14] G. J. Hutchings, "Selective oxidation using gold and gold-palladium nanoparticles.," in *Turning Points Solid-State, Mater. Surf. Sci.*, pp. 550–567, Royal Society of Chemistry, 2008.

[15] G. J. Hutchings, "Nanocrystalline gold and gold palladium alloy catalysts for chemical synthesis," *Chemical communications (Cambridge, England)*, no. 10, pp. 1148–64, 2008.

[16] G. J. Hutchings, "Nanocrystalline gold catalysts: a reflection on catalyst discovery and the nature of active sites.," *Gold Bulletin (London, United Kingdom)*, vol. 42, no. 4, pp. 260–266, 2009.

[17] G. J. Hutchings, "Heterogeneous catalysts-discovery and design.," *Journal of Materials Chemistry*, vol. 19, no. 9, pp. 1222–1235, 2009.

[18] P. C. Della, E. Falletta, L. Prati, and M. Rossi, "Selective oxidation using gold," *Chemical Society reviews*, vol. 37, no. 9, pp. 2077–95, 2008.

[19] T. Matsumoto, M. Ueno, N. Wang, and S. Kobayashi, "Recent advances in immobilized metal catalysts for environmentally benign oxidation of alcohols," *Chemistry, an Asian journal*, vol. 3, no. 2, pp. 196–214, 2008.

[20] N. Dimitratos, J. A. Lopez-Sanchez, and G. J. Hutchings, "Green Catalysis with Alternative Feedstocks.," *Topics in Catalysis*, vol. 52, no. 3, pp. 258–268, 2009.

[21] M. Boronat and A. Corma, "Oxygen activation on gold nanoparticles: separating the influence of particle size, particle shape and support interaction," *Dalton Trans.*, vol. 39, no. 36, pp. 8538–8546, 2010.

[22] M. Boronat, A. Corma, F. Illas, J. Radilla, T. Rdenas, and M. J. Sabater, "Mechanism of selective alcohol oxidation to aldehydes on gold catalysts: Influence of surface roughness on reactivity," *Journal of Catalysis*, vol. 278, pp. 50–58, Feb. 2011.

[23] J.-H. Liu, A.-Q. Wang, Y.-S. Chi, H.-P. Lin, and C.-Y. Mou, "Synergistic effect in an Au-Ag alloy nanocatalyst: CO oxidation," *The journal of physical chemistry. B*, vol. 109, no. 1, pp. 40–3, 2005.

[24] J. Zhang, Y. Jin, C. Li, Y. Shen, L. Han, Z. Hu, X. Di, and Z. Liu, "Creation of three-dimensionally ordered macroporous Au/CeO2 catalysts with controlled pore sizes and their enhanced catalytic performance for formaldehyde oxidation.," *Applied Catalysis, B: Environmental*, vol. 91, no. 1-2, pp. 11–20, 2009.

[25] H.-L. Jiang, T. Akita, T. Ishida, M. Haruta, and Q. Xu, "Synergistic catalysis of Au@Ag core-shell nanoparticles stabilized on metal-organic framework," *Journal of the American Chemical Society*, vol. 133, no. 5, pp. 1304–6, 2011.

[26] R. Ferrando, J. Jellinek, and R. L. Johnston, "Nanoalloys: From Theory to Applications of Alloy Clusters and Nanoparticles," *Chemical Reviews*, vol. 108, pp. 845–910, Mar. 2008.

[27] G. Bozzolo, J. E. Garces, and G. N. Derry, "Atomistic modeling of segregation and bulk ordering in Ag Au alloys," *Surface Science*, vol. 601, pp. 2038–2046, May 2007.

[28] K. Kim, K. L. Kim, J.-Y. Choi, H. B. Lee, and K. S. Shin, "Surface enrichment of Ag atoms in Au/Ag alloy nanoparticles revealed by Surface-Enhanced Raman Scattering of 2,6-dimethylphenyl isocyanide.," *Journal of Physical Chemistry C*, vol. 114, no. 8, pp. 3448–3453, 2010.

[29] C. H. Christensen, B. Joergensen, J. Rass-Hansen, K. Egeblad, R. Madsen, S. K. Klitgaard, S. M. Hansen, M. R. Hansen, H. C. Andersen, and A. Riisager, "Formation of acetic acid by aqueous-phase oxidation of ethanol with air in the presence of a heterogeneous gold catalyst.," *Angewandte Chemie, International Edition*, vol. 45, no. 28, pp. 4648–4651, 2006.

[30] L. Prati and M. Rossi, "Gold on carbon as a new catalyst for selective liquid phase oxidation of diols.," *Journal of Catalysis*, vol. 176, no. 2, pp. 552–560, 1998.

[31] B. Jorgensen, S. Egholm, Christiansen, M. L. Dahl, Thomsen, and C. H. Christensen, "Aerobic oxidation of aqueous ethanol using heterogeneous gold catalysts: Efficient routes to acetic acid and ethyl acetate.," *Journal of Catalysis*, vol. 251, no. 2, pp. 332–337, 2007.

[32] C. Marsden, E. Taarning, D. Hansen, L. Johansen, S. K. Klitgaard, K. Egeblad, and C. H. Christensen, "Aerobic oxidation of aldehydes under ambient conditions using supported gold nanoparticle catalysts.," *Green Chemistry*, vol. 10, no. 2, pp. 168–170, 2008.

[33] T. Takei, N. Iguchi, and M. Haruta, "Support effect in the gas phase oxidation of ethanol over nanoparticulate gold catalysts.," *New Journal of Chemistry*, vol. 35, no. 10, pp. 2227–2233, 2011.

[34] R. Zanella, S. Giorgio, C. R. Henry, and C. Louis, "Alternative Methods for the Preparation of Gold Nanoparticles Supported on TiO2.," *Journal of Physical Chemistry B*, vol. 106, no. 31, pp. 7634–7642, 2002.

[35] R. Zanella, E. V. Basiuk, P. Santiago, V. A. Basiuk, E. Mireles, I. Puente-Lee, and J. M. Saniger, "Deposition of Gold Nanoparticles onto Thiol-Functionalized Multiwalled Carbon Nanotubes.," *Journal of Physical Chemistry B*, vol. 109, no. 34, pp. 16290–16295, 2005.

[36] R. Zanella, L. Delannoy, and C. Louis, "Mechanism of deposition of gold precursors onto TiO2 during the preparation by cation adsorption and deposition-precipitation with NaOH and urea.," *Applied Catalysis, A: General*, vol. 291, no. 1-2, pp. 62–72, 2005.

[37] R. Zanella and C. Louis, "Influence of the conditions of thermal treatments and of storage on the size of the gold particles in Au/TiO2 samples.," *Catalysis Today*, vol. 107-108, pp. 768–777, 2005.

[38] M. Campanati, G. Fornasari, and A. Vaccari, "Fundamentals in the preparation of heterogeneous catalysts," *Catalysis Today*, vol. 77, pp. 299–314, Jan. 2003.

[39] D. Ulrike, "The surface science of titanium dioxide," *Surface Science Reports*, vol. 48, pp. 53–229, Jan. 2003.

[40] B. Bachiller-Baeza, I. Rodriguez-Ramos, and A. Guerrero-Ruiz, "Interaction of Carbon Dioxide with the Surface of Zirconia Polymorphs," *Langmuir*, vol. 14, no. 13, pp. 3556–3564, 1998.

[41] G. A. Parks, "The Isoelectric Points of Solid Oxides, Solid Hydroxides, and Aqueous Hydroxo Complex Systems," *Chemical Reviews*, vol. 65, no. 2, pp. 177–198, 1965.

[42] S. R. Bare and T. Ressler, "Chapter 6 Characterization of Catalysts in Reactive Atmospheres by X-ray Absorption Spectroscopy," vol. Volume 52, pp. 339–465, Academic Press, 2009.

[43] D. Koningsberger, B. Mojet, G. van Dorssen, and D. Ramaker, "XAFS spectroscopy; fundamental principles and data analysis," *Topics in Catalysis*, vol. 10, no. 3, pp. 143–155, 2000-05-01.

[44] B. J. Hwang, S. M. S. Kumar, C.-H. Chen, R.-W. Chang, D.-G. Liu, and J.-F. Lee, "Size and alloying extent dependent physiochemical properties of Pt-Ag/C nanoparticles synthesized by the ethylene glycol method.," *Journal of Physical Chemistry C*, vol. 112, no. 7, pp. 2370–2377, 2008.

[45] "http://www.cheric.org/research/kdb/hcprop/showcoef.php?cmpid=818&prop=PVP."

[46] B. Ravel and M. Newville, "ATHENA, ARTEMIS, HEPHAESTUS: data analysis for X-ray absorption spectroscopy using IFEFFIT," *Journal of Synchrotron Radiation*, vol. 12, no. 4, pp. 537–541, 2005.

[47] T. V. Janssens, A. Carlsson, A. Puig-Molina, and B. S. Clausen, "Relation between nanoscale Au particle structure and activity for CO oxidation on supported gold catalysts," *Journal of Catalysis*, vol. 240, pp. 108–113, June 2006.

[48] K. Kainz, "Wahlpraktikum Realkatalyse," tech. rep., IMC TU Wien, 2011.

[49] A. Sandoval, A. Aguilar, C. Louis, A. Traverse, and R. Zanella, "Bimetallic Au-Ag/TiO2 catalyst prepared by deposition-precipitation: High activity and stability in CO oxidation.," *Journal of Catalysis*, vol. 281, no. 1, pp. 40–49, 2011.

[50] M. G. Newville, *Local Thermodynamic Measurements of Dilute Binary Alloys Using XAFS*. PhD thesis, University of Washington, 1995.

[51] A. I. Frenkel, V. S. Machavariani, A. Rubshtein, Y. Rosenberg, A. Voronel, and E. A. Stern, "Local structure of disordered Au-Cu and Au-Ag alloys," *Phys. Rev. B*, vol. 62, pp. 9364–, Oct. 2000.

[52] K. I. Hadjiivanov and G. N. Vayssilov, "Characterization of oxide surfaces and zeolites by carbon monoxide as an IR probe molecule," vol. Volume 47, pp. 307–511, Academic Press, 2002.

[53] F. Boccuzzi, A. Chiorino, M. Manzoli, D. Andreeva, T. Tabakova, L. Ilieva, and V. Iadakiev, "Gold, silver and copper catalysts supported on TiO2 for pure hydrogen production," *Catalysis Today*, vol. 75, pp. 169–175, July 2002.

[54] H. Hartshorn, C. J. Pursell, and B. D. Chandler, "Adsorption of CO on Supported Gold Nanoparticle Catalysts: A Comparative Study.," *Journal of Physical Chemistry C*, vol. 113, no. 24, pp. 10718–10725, 2009.

[55] F. Boccuzzi, A. Chiorino, S. Tsubota, and M. Haruta, "FTIR Study of Carbon Monoxide Oxidation and Scrambling at Room Temperature over Gold Supported on ZnO and TiO2. 2," *The Journal of Physical Chemistry*, vol. 100, pp. 3625–3631, Jan. 1996.

[56] S. Tanuma, C. J. Powell, and D. R. Penn, "Calculations of electorn inelastic mean free paths. II. Data for 27 elements over the 50-2000 eV range," *Surf. Interface Anal.*, vol. 17, no. 13, pp. 911–926, 1991.